

**Reduced-Dimensional Retrievals of Precipitation from the
TRMM Microwave Imager: Physical Insight and Information
Content**

BY

Ke Li

M.S., Mechanical Engineering, University of New Hampshire (2010)

A thesis submitted
in partial fulfillment of
the requirements for the degree of

Master of Science
(Atmospheric Sciences)

at the

UNIVERSITY OF WISCONSIN-MADISON

2013

This thesis has been examined and approved.

Thesis director, Grant Petty
Professor of University of Wisconsin–Madison

Tristan L'ecuyer
Assistant Professor of University of Wisconsin–Madison

Ralf Bennartz
Professor at University of Wisconsin–Madison

Date

Dedication

To our God, the creator ...

The breath of God produces ice,
and the broad waters become frozen.
He loads the clouds with moisture;
he scatters his lightning through them.
At his direction they swirl around
over the face of the whole earth
to do whatever he commands them.
He brings the clouds to punish people,
or to water his earth and show his love.
—Job 37:10-13, NIV Bible

Acknowledgments

This thesis is written as completion to the Master of Science in Atmospheric and Oceanic Sciences, at the University of Wisconsin–Madison. The master program focuses on the microwave remote sensing in terms tropical rain rate retrieval algorithm development. The subject of the this thesis, Reduced-Dimensional Retrievals of Precipitation from the TRMM Microwave Imager: Physical Insight and Information Content, is intended to examine:

- To retrieve rain rate, what are the three most significant physical features of a storm observed by the microwave imagers of satellite TRMM?
- How important are each observed features in terms of retrieving rain rates?

I want to thank my supervisor, Prof. Grant Petty, of being great help during the development of this thesis. Besides, though my 2.5 year graduate study, Prof. Grant Petty to the best demonstrates to me as a good example of professional scientist with his innovative mind and hard-working spirit.

Moreover, as a friend and mentor, Prof. Grant Petty guided me with patience and humility, provided me with confirmations and useful critiques, and shared with me about life philosophy using information theories:

“Different from echoing, confirmation can only be counted as confirmation when there’s a chance of disagreement.”

—Dr. Grant Petty

I’d like also give thanks to Prof. Larissa Back and Prof. Jonathan Martin for their instructions and critiques. It was their presence that makes me grow as a young researcher with

even stronger faith. It was their feedback that inspired me to develop further my project to a deeper level.

“As iron sharpens iron, so one person sharpens another”

—Proverbs 27:17, NIV Bible

I'd like to thank Prof. Tristan L'ecuyer for his time and effort on giving me feedback of my project. I'd like to thank the PhD student Alex Matus, Pei Wang, the MS student Kyle Hosley, Marc Collins, William Line, Kuniaki Inoue, and Bryan Crouch. It was their friendship that fills my office life with a lots of joy! Besides, it is their comments and critiques in the daily conversation that motivated me to make improvement on my projects.

Especially, I want to thank my wife, Kristen, for her dedicated commitment with me at ups and downs during my graduate study in UW–Madison. I deeply appreciate her strong spiritual support, in terms of prayers, encouragement, and comforting, which constantly remind of me of my integrity and faith to be a good man. Besides, I'd like to thank my wife, Kristen, for every single meals she prepared for me in the midst of my busy study. I'd like to thank her also for all the effort that she did to keep me relaxed and cheered after a busy day: watching Madagascar 3, having hot dates at the Walmart or the McDonald, and having random game nights, etc. Without her support and companionship, I can hardly reach today's achievement.

I also want to thank my small group from Faith Community Bible Church for their wisdom and prayers. It was their constant love and prayers that keep me on track of my conviction as a Christian man. It was their warm hearts that made Madison WI a cozy home for me during my graduate study.

Most importantly, I want to give my highest praise and appreciation to our omnipotent God, creator of the universe. It is by his grace my sin is forgiven, and my debt is paid. It is his enduring love that breaks all the chains of my life and sets me free. It is his power that turns ugliness into beauty. It is His righteousness and patience through Jesus Christ that influences me daily to move forward with my new identity.

Table of Contents

Dedication	i
Acknowledgments	ii
Abstract	xiv
1 Introduction	1
1.1 Historical Overview	1
1.1.1 Experimental basis before 1978	1
1.1.2 SMMR in 1978	2
1.1.3 SSM/I in 1987	3
1.1.4 TRMM in 1997	5
1.1.5 GPM in 2014	6
1.2 Retrieval Methodology	7
1.2.1 Cloud Resolving Models	7
1.2.2 Screening	7
1.2.3 Bayesian estimation methods	8
1.3 Information Theory	12
1.3.1 Shannon Entropy	12
1.3.2 Relative Entropy	13
1.4 Objectives	15
2 Passive Microwave Sensors and Rain Rate Retrieval	17
2.1 Brightness Temperatures	18

2.1.1	Emission	18
2.1.2	Transmittance	19
2.1.3	Radiative Transfer Equations	19
2.1.4	Earth Surface Types	22
2.1.5	Cloud and Rain Water Emission and Ice Scattering	24
2.1.6	Polarization and Rain Rate	28
2.2	Bayesian Algorithm for Rain Rate Retrieval	31
3	Pseudo-channels	34
3.1	Over the Ocean	34
3.1.1	Gram-Schmidt Process	35
3.1.2	CH1	38
3.1.3	CH2	38
3.1.4	CH3	39
3.2	Probability Distribution Functions	40
4	Information Theory	46
4.1	Shannon Entropy and Relative Entropy	46
4.1.1	Gaussian Distribution	46
4.2	Pseudo-channels	50
4.3	Necessity	61
4.3.1	CH1	61
4.3.2	CH2	68
4.3.3	CH3	74
4.4	Sufficiency	79
5	Conclusions	83

List of Tables

2.1	Surface type descriptions in Figure 2-5 (Petty and Li, 2013a)	25
3.1	Case division for Gram-Schmidt analysis	38
4.1	Maximum retrieved rain rate changes in posterior probability distributions by adding CH1 under various surface types. The columns are denoted as (from left to right): surface categories, surface skin temperature, total precipitable water, CH1, rain rate difference (posterior - prior), rain rate ratio (posterior/prior), probability of posterior rain rate equal to zero mm/hr, probability of posterior rain rate greater than 1 mm/hr, relative entropy, and Shannon entropy difference. The threshold of sample numbers in this analysis is 1000 samples. All cases in 4c have less than the threshold, therefore, the 4c cases cannot be considered statistically representative.	67

- 4.2 Maximum retrieved rain rate changes in posterior probability distributions by adding CH2 under various surface types. The columns are denoted as (from left to right): surface categories, surface skin temperature, total precipitable water, CH1, CH2, rain rate difference (posterior - prior), rain rate ratio (posterior/prior), probability of posterior rain rate equal to zero mm/hr, probability of posterior rain rate greater than 0.1 mm/hr, relative entropy, and Shannon entropy difference. The threshold of sample numbers in this analysis is 1000 samples. All cases in 4c have less than the threshold, therefore, the 4c cases cannot be considered statistically representative. 73
- 4.3 Maximum retrieved rain rate changes in posterior probability distributions by adding CH3 under various surface types. The columns are denoted as (from left to right): surface categories, surface skin temperature, total precipitable water, CH1, CH2, CH3, rain rate difference (posterior - prior), rain rate ratio (posterior/prior), probability of posterior rain rate equal to zero mm/hr, probability of posterior rain rate greater than 0.01 mm/hr, relative entropy, and Shannon entropy difference. The threshold of sample numbers in this analysis is 1000 samples. All cases in 4c have less than the threshold, therefore, the 4c cases cannot be considered statistically representative. 78

List of Figures

1-1	Data for postboost TMI sensors in various frequencies, including polarization (V is vertically polarized, H is horizontally polarized.), instantaneous field of view (IFOV), etc. (Kummerow, 2006)	16
2-1	Passive microwave remote sensing mechanism. Green arrows are radiance reflected by the earth. Blue arrows are radiance emitted directly by the atmosphere. The gray dotted arrow represents radiance emitted directly from the earth surface. T_A is the averaged atmospheric temperature. T_s is the surface temperature. ε is the surface emissivity. t is the transmittance of the atmosphere.	23
2-2	Land ocean brightness temperature difference reflected in the image of AMSR-E 10 GHz V on the west coast of US. (Courtesy to U.S.Navy/NRL/NASA)	25
2-3	Map of brightness temperature differences, 10 GHz(V) - 10 GHz(H) for 2002 TMI non-precipitating pixels.	26
2-4	Map of brightness temperature of 85 GHz(H) for 2002 TMI non-precipitating pixels.	26
2-5	Map of the seven surface classes constructed by using TMI brightness temperatures for 2002. (Petty and Li, 2013a)	26

2-6	Typical response of different TRMM channels to rain rate. Red dots are 10 GHz. Blue dots are 19 GHz. Magenta dots are 37 GHz. Green dots are 85 GHz. The horizontal axis is retrieved rain rate, not directly measured PR rain rate. The plots here serve to illustratively show the trends of brightness temperatures. Using retrieved rain rate would have more samples that represent trends of TMI brightness temperatures. .	29
2-7	Scattering plots of polarizations with rain rate under TMI channel: (upper, left) 10 GHz, (upper, right) 19 GHz, (bottom, left) 37 GHz, (bottom, right) 85 GHz. Horizontal axes are brightness temperatures of vertically polarized channels, and vertical axes are brightness temperatures of horizontally polarized channels.	30
2-8	Comparisons of algorithms and PR rain rate data. (Left) comparison between PR rainfall rate and rainfall retrieved in 2A12; and (Right) comparison between PR rainfall rate and rainfall retrieved with UW algorithm. (Petty and Li, 2013a)	33
3-1	Scatter plots of three pseudo-channels over the ocean (1B11.20020911.27506.7.HDF): (a) CH1 and CH2, (b) CH3 and CH2, and (c) CH1 and CH3. The blue line refers to the division of different cases for Gram-Schmidt analysis	37
3-2	Orthogonal modes of 9-microwave-channel distributions with: CH1 positive in blue dotted line, CH2 positive in green triangles, CH2 negative in black triangles, CH3 positive in magenta squares, and CH3 negative in red diamond.	43

3-3	Microwave channels 19GHz V, 85GHz V, and retrieve rain rate of Hurricane Lily in October 2002, to the southwest of Florida. (a) 19GHz V brightness temperature (K), (b) 85GHz V brightness temperature (K), and (c) retrieved rain rate in mm/hr.	44
3-4	Pseudo-channels of Hurricane Lily in October 2002, to the southwest of Florida. (a) CH1, (b) CH2, (c) CH3, and (d) RGB plot of CH1 (red), CH2 (green), and CH3 (blue).	45
4-1	Information entropy changes between two Gaussian distributions over unevenly divided bins. Blue blocks are normal distribution before, and pink blocks are normal distribution afterwards. All upper panels are probability density functions (PDFs), and lower panels are changes of informational entropy of different kinds. The green lines are continuous Shannon entropy difference (ΔCSE). The magenta lines are discrete Shannon entropy difference (ΔDSE). The cyan lines are relative entropy (RE).	56
4-2	Information entropy changes between two Gaussian distributions over evenly divided bins. Blue blocks are normal distribution before, and pink blocks are normal distribution afterwards. All upper panels are probability density functions (PDFs), and lower panels are changes of informational entropy of different kinds. The magenta lines are discrete Shannon entropy difference (ΔDSE). The cyan lines are relative entropy (RE).	57

- 4-3 Probability distribution changes and information entropy changes with restrictions of CH1, CH2, and CH3. The land type is 0w. After scaling, $T_{\text{skin}} = 6$, $\sigma_{\text{water}} = 7$, CH1 = 41, CH2 = 38, CH3 = 23. Color blocks are probability within each bin, using the vertical axis to the left. The black triangle lines are relative entropy (RE). The black dotted lines are change of shannon entropy ΔSE . Both triangle and dotted lines follow the vertical coordinates to the right. Shown in each panels are: (a) only climate data, (b) climate data with CH1 restriction, (c) climate data with restrictions of CH1 and CH2, and (d) climate data with restrictions of CH1, CH2, and CH3. 58
- 4-4 Probability distribution changes and information entropy changes with restrictions of CH1, CH2, and CH3. The land type is 0w. After scaling, $T_{\text{skin}} = 3$, $\sigma_{\text{water}} = 2$, CH1 = 23, CH2 = 27, CH3 = 23. Color blocks are probability within each bin, using the vertical axis to the left. The black triangle lines are relative entropy (RE). The black dotted lines are change of shannon entropy ΔSE . Both triangle and dotted lines follow the vertical coordinates to the right. Shown in each panels are: (a) only climate data, (b) climate data with CH1 restriction, (c) climate data with restrictions of CH1 and CH2, and (d) climate data with restrictions of CH1, CH2, and CH3. 59

4-5	Probability distribution changes and information entropy changes with restrictions of CH1, CH2, and CH3. The land type is 0w. After scaling, $T_{\text{skin}} = 4$, $\sigma_{\text{water}} = 1$, CH1 = 23, CH2 = 23, CH3 = 26. Color blocks are probability within each bin, using the vertical axis to the left. The black triangle lines are relative entropy (RE). The black dotted lines are change of shannon entropy ΔSE . Both triangle and dotted lines follow the vertical coordinates to the right. Shown in each panels are: (a) only climate data, (b) climate data with CH1 restriction, (c) climate data with restrictions of CH1 and CH2, and (d) climate data with restrictions of CH1, CH2, and CH3.	60
4-6	Rain rate information change by adding CH1 restriction. (a) average rain rate (R) difference, (b) average rain rate ratio, (c) probability of $R = 0$, (d) probability of $R > 1\text{mm hr}^{-1}$, (e) relative entropy after adding CH1, and (f) Shannon entropy difference after adding CH1. The land type is 0w. Environmental variables: $T_{\text{skin}} = 6$, $\sigma_{\text{water}} = 6$ after scaling.	64
4-7	Same as above. The land type is 1w. Environmental variables: $T_{\text{skin}} = 5$, $\sigma_{\text{water}} = 6$ after scaling.	66
4-8	Rain rate information change by adding CH2 restriction. (a) average rain rate (R) difference, (b) average rain rate ratio, (c) probability of $R = 0$, (d) probability of $R > 1\text{mm hr}^{-1}$, (e) relative entropy after adding CH2, and (f) Shannon entropy difference after adding CH2. The land type is 0w. Environmental variables: $T_{\text{skin}} = 6$, $\sigma_{\text{water}} = 6$ after scaling.	71
4-9	Same as above. The land type is 1w. Environmental variables: $T_{\text{skin}} = 5$, $\sigma_{\text{water}} = 6$	72

4-10	Rain rate information change by adding CH3 restriction. (a) average rain rate (R) difference, (b) average rain rate ratio, (c) probability of $R = 0$, (d) probability of $R > 1\text{mm hr}^{-1}$, (e) relative entropy after adding CH3, and (f) Shannon entropy difference after adding CH3. The land type is 0w. CH1 = 24, Environmental variables: $T_{\text{skin}} = 4$, $\sigma_{\text{water}} = 3$ after scaling.	75
4-11	Same as above. The land type is 1w. CH1 = 24, Environmental variables: $T_{\text{skin}} = 6$, $\sigma_{\text{water}} = 6$ after scaling.	77
4-12	Bivariate histograms comparing distributions of rain rates prior to (horizontal axis) and following (vertical axis) the successive addition of channels, starting with Channel 1 relative to climatology (left), Channel 1+2 relative to Channel 1 only (center), Channels 1-3 relative to 1+2 (right). The surface type here is ocean (0w).	81
4-13	Same as above. The surface type here is warm vegetated land (1w).	81
4-14	Same as above. The surface type here is warm land/water mix, coast (2w).	82
4-15	Same as above. It includes all surface types (0w, 1w, 1c, 2w, 2c, 3w, 3c, 4w, 4c, 5w, 5c, 6w, 6c), where surface 4c has zero selected samples for the statistics that are statistically representative.	82

ABSTRACT

Reduced-Dimensional Retrievals of Precipitation from the TRMM Microwave Imager: Physical Insight and Information Content

by

Ke Li

University of Wisconsin-Madison, , 2013

The TRMM Microwave Imager (TMI) is employed to observe and measure tropical rainfall using information from nine passive microwave channels. These channels are sensitive not only to rainfall but also to clouds, water vapor, ice, surface moisture, and snow cover, among other variables. These other variables are a noise source in the retrieval of precipitation. Petty (2012) has devised a dimensional reduction algorithm that filters out much of the background noise while retain much of the precipitation information in the form of three so-called pseudo-channels, which are constructed as linear combinations of the original nine channels. The purpose of the present work is to investigate the nature of the physical information about storm structure contained in each of the pseudo-channels and to examine their combined utility in revealing subtle differences between precipitating cloud systems in different environments.

Chapter 1

Introduction

1.1 Historical Overview

Rain rate retrieval from satellite has been moving forward mainly according to the technology improvement for radiometers.

1.1.1 Experimental basis before 1978

In the early 1970s, a few passive microwave sensors were used for precipitation estimation research. Both Nimbus-5 launched in 1972 and Nimbus-6 launched in 1976 had the Electronic Scanning Microwave Radiometer [ESMR, Wilheit (1972)] on board. ESMR on Nimbus-5 platform had only one channel, 19 GHz, horizontally polarized, with a resolution of 25 km. The swath width is 160 km. ESMR on Nimbus-6 platform had two channels, 37 GHz, horizontally and vertically polarized.

One of the earliest quantitative rain rate estimations was built by Wilheit et al. (1977), who associated the change of brightness temperature of 19 GHz on Nimbus-5 over the ocean with surface rain rate variation. Wilheit et al. (1977) utilized rain gauge and radar observations to verify the assumption. The rain rate was calculated from radar observations (Marshall and Palmer, 1948). The ocean was observed to be a cold background in brightness temperature of 19 GHz. For moderate rain rate $1 \sim 20 \text{ mm hr}^{-1}$, the brightness temperature warms up. At high rain rates ($> 20 \text{ mm hr}^{-1}$),

brightness temperature of 19 GHz was observed to reach ‘saturation’, due to the enhanced scattering of ice aloft.

Another one of quantitative rain rate estimations was built by Weinman and Guetter (1977), who associate the change of brightness temperature difference between vertical and horizontal polarizations of 37 GHz on Nimbus-6 over the ocean and land with rain rate. The water surface was observed to have strong polarization compared with land at 37 GHz. When precipitation was added to the water background, brightness temperatures was observed to be weakly polarized. A ‘Polarization correction’ was defined to eliminate contrast between water and land as background noise in rain rate retrieval. Simple form in noise filtering among surface types was widely used in later rain rate retrieval algorithms (Spencer et al., 1989; Conner and Petty, 1998; Kidd, 1998).

1.1.2 SMMR in 1978

In 1978, two copies of the Scanning Multichannel Microwave Radiometer (SMMR) were launched, on the Seasat-A oceanographic satellite and the Nimbus-7 meteorological satellite (Gloersen and Barath, 1977). The first of these failed 3 months after launch; while the Nimbus 7 SMMR continued to function for nine years. SMMR was the most advanced microwave radiometer launched to that time. SMMR has ten channels at frequencies at 6.6, 10.7, 18.0, 21.0, and 37.0 GHz with horizontal and vertical polarizations each. SMMR was intended to obtain ocean and atmospheric parameters (ex. sea surface temperatures, low altitude winds, water vapor and cloud liquid water content). The Nimbus 7 SMMR was decommissioned in 1987.

Examining SMMR data, (Spencer et al., 1983) addressed three most basic and quite influential concepts on physical-based rain rate retrieval algorithm for later literatures. First, cold brightness temperature at 37 GHz was observed in heavy

rainfall events over land. Brightness temperatures on SMMR include contributions not only due to liquid phase atmospheric constituents, but also due to ice phase atmospheric constituents. Due to this observation, rain rate retrievals were conceptually divided into two parts: emission based algorithm, where warm and nonpolarized liquid phase atmospheric constituents were seen against cold and polarized water surface background; and scattering based algorithms, where cold and weakly polarized ice phase atmospheric constituents were seen against cold and polarized water surface background or warm and weakly polarized land surface. The similar observation associating surface rain rate with intensity of brightness temperature depression due to ice scattering was addressed in Wilheit (1986). Third, rain rate retrieval biases due to partially filled fields of views (FOVs) was observed in Spencer et al. (1983), which was later named as ‘beaming filling effect’ (Kummerow, 1998; Kummerow and Poyner, 2004; Petrenko, 2001; Petty, 1994a,b; Chiu et al., 1990; Ha and North, 1995). These three basic observations regarding microwave brightness temperatures and rain rate dominated mainstream thinking about the retrieved problem for many years.

1.1.3 SSM/I in 1987

On June 19th, 1987, the first Special Sensor Microwave/Image (SSM/I) was launched on the F-8 satellite (Block 5D-2 model) in the Defense Meteorological Satellite Program (DMSP). The goal of SSM/I was to provide the Navy and Air Force with operational imagery of weather systems and remote sensing data on critical surface and atmospheric parameters. The F-8 satellite was set to travel in a near polar (98.8°) circular (± 7 m) sun-synchronous orbit. With an altitude of 833km has microwave channels of 19.35, 22.235, 37.0 and 85.5 GHz (Hollinger, 1989). Most of the SSM/I microwave channels are dual polarized with vertical and horizontal directions, except 22 GHz. In SSM/I, the new channel 85 GHz was added which reflects higher

sensitivity to ice scattering as well as higher resolution.

Spencer et al. (1989) pointed out that 85 GHz shows small polarization over an optically thick precipitating hydrometeor, and large polarization over the ocean surface. He defined the so called ‘Polarization corrected temperature’ (PCT) and used it to distinguish strong ice scattering from emission due to liquid clouds and precipitation. The PCT was pointed out to reflect the intensity of scattering by ice without the influence of background noise, and the column optical depth.

As new algorithms for SSM/I were developed by numerous investigators (Wilheit et al., 1991; Liu and Curry, 1992; Prabhakara et al., 1992; Kummerow and Giglio, 1994b; Petty, 1994b; Ferraro et al., 1996; Wentz, 1998; Schols et al., 1999; Prigent et al., 2001), a number of validation and intercomparison exercises were undertaken, including the Precipitation Intercomparison Projects (PIP1–3) (Barrett et al., 10–14 Jul. 1995; Smith et al., 1998; Adler et al., 2001) and the Global Precipitation Climatology Project (GPCP) Algorithm Intercomparison Projects (AIP1–3). PIP1–3 performed regional estimated rain fall comparison, over land and ocean. AIP1–3 focuses on improve algorithm by merging products. Comparisons were also made between PIP1–3 and AIP1–3 by Ebert et al. (1996); Barrett et al. (10–14 Jul. 1995); Smith et al. (1998); Adler et al. (2001); Schols et al. (1999) etc.

Petty (1994a,b) pointed out that SSM/I over the ocean reflects different degree of three components: emission from atmospheric liquid water and gaseous absorbers, featured with “warm” and weakly polarized Tbs, scattering due to ice-phase precipitation, featured with “cold” and weakly polarized Tbs, and polarized ocean surface background, featured with “cold” and strongly polarized Tbs.

Further, two parameters were composed in (Petty, 1994a,b), to quantitatively reveal the two most important cloud features strongly associated with rain rates: depolarization due to cloud liquid water from highly polarized ocean surface, measured

by normalized polarization difference P , and ice scattering from top of a precipitating cloud, measured by volume scattering index S . The parameter P is described as:

$$P \equiv \frac{T_V - T_H}{T_{V,O} - T_{H,O}} \quad (1.1)$$

where T_V and T_H are the observed vertical and horizontal polarized brightness temperatures at the same frequency; and $T_{V,O}$ and $T_{H,O}$ are the vertical and horizontal polarized brightness temperatures of the same frequency at the same scene without the clouds. The parameter S is described as:

$$S = PT_{V,O} + (1 - P)T_c - T_V \text{ or, } S = PT_{H,O} + (1 - P)T_c - T_H \quad (1.2)$$

where, T_c is the (unpolarized) limiting brightness temperature as a hypothetical non-scattering liquid water layer becomes optically thick, which is suggested to be $T_c = 273$ K.

1.1.4 TRMM in 1997

The Tropical Rainfall Measuring Mission (TRMM) was launched on November 27, 1997, with precipitation radar (PR) and TRMM microwave imager (TMI). The TRMM scans the earth averagely 16 times a day at a marching speed of 6.9 km/s, covering $38^\circ\text{S} \sim 38^\circ\text{N}$, the tropical region and some subtropical regions. The TMI measures the intensity of radiation at five separate frequencies 10.7, 19.4, 21.3, 37, and 85.5 GHz with both vertical and horizontal polarizations, except 21.3 GHz only has vertical polarization. The TMI has a swath width of 880 km on the surface. The TMI has swath of 104 pixels per scan for channels of 10.7, 19.4, 21.3, and 37 GHz, and 208 pixels for channels of 85 GHz (Simpson et al., 1988; Kummerow et al., 1998, 2000). Regarding the scanning geometry, the TMI has off-nadir incident angle of 52.8° and conical scan of 130° . The PR has nadir scanning with a swath of 215 km. The nine TMI channels are set to have different of field of views (FOVs, in 1-1).

TRMM experienced a satellite reposition in August 2001, which divides the life of TRMM into preboost and postboost. The preboost started on December 8th, 1997, and ended on August 7th, 2001. During the preboost, the swath width of TMI was 760 km. The spatial resolution is 4.4km at 85.5 GHz. The postboost started on August 24th, 2001 and is still on going. The swath width of TMI during postboost period is 878 km. The spatial resolution is 5.1 km at 85.5 GHz. Other variables regarding TMI channels are presented in Table 1-1.

The installation of first spaceborne weather radar made the TMI and PR complementary in terms of surface rain rate retrieval (Haddad et al., 1997; Grecu and Anagnostou, 2002; Grecu et al., 2004; Grecu and Olson, 2006). The most recent algorithms have been confined to Bayesian estimation methods, which will be introduced in later sections. In particular, the Goddard Profiling algorithm (GPROF) (Kummerow et al., 2001, 2006, 2007, 2011) has become the standard operational algorithm for TMI and will continually be refined for GMI for Global Precipitation Measurement (GPM) mission. The earlier versions of GPROF (Kummerow et al., 2001, 2006) depended on a database constructed from simulation derived from cloud resolving models. However, progress has been made in the later version of GPROF Kummerow et al. (2011) that avoided both cloud resolving models and screening.

1.1.5 GPM in 2014

The Global Precipitation Measurement (GPM) mission is designed to carry an advanced radar and radiometer system to measure the global precipitation. The GPM Core Observatory will have a Dual-frequency Precipitation Radar (DPR) and a multi-channel GPM Microwave Imager (GMI) (Smith et al., 2007). Equipped with DPR, GPM can provide new information about particle drop size distribution over moderate precipitation intensities. The new features of GPM will provide measurement for

research about human activity influencing precipitation. Similar to TMI, GMI will have horizontal and vertical polarizations across the 10.7 ~ 89 GHz spectrum, and possibly 3–5 additional high frequency channels positioned at 166 GHz and 183 GHz. Regarding scan geometry, GMI will have swath width of 885 km, off-nadir incident angle of 52.8° , and conical scan range of 140° . The DPR will have nadir scanning with swath width of 215 km for Ku-band radar and 245 km for Ka-band radar. The DPR will have spatial resolution of 5 km. The core of GPM is scheduled for launch in early 2014.

1.2 Retrieval Methodology

1.2.1 Cloud Resolving Models

For the past twenty years, convective-scale models have greatly improved the study of dynamics and microphysics of mesoscale convective systems. Modern cloud resolving models are non-hydrostatic and include an explicit representation of microphysical processes (Kummerow et al., 2001, 2007, 2011). In several studies, (Panegrossi et al., 1998; Adler et al., 2001; Aonashi et al., 1996), algorithms based on cloud resolving models have been validated. It was pointed out that the precision of rain rate retrieval largely depends on the quality of the cloud resolving models and associated radiative transfer assumptions.

1.2.2 Screening

Screening is a modification methodology to improve the consistency between rainfall estimates from different sensors. Screening was firstly addressed in more completed details by Ferraro et al. (1998), for rain/no rain identification. In microwave precipitation retrieval over land, screening serves to make a decision whether the observed

signature reflects the rain condition or specific land type that shares the similar observed signature (Sudradjat et al., 2011). The Grody-Ferraro screening methodology (Ferraro et al., 1998; Grody, 1991) is frequently applied, and was employed within GPROF (Kummerow et al., 2001).

Used in some prior precipitation retrieval algorithms, screening is set to conceptually categorize non-rain scenarios from rain scenarios, or categorize stratiform precipitation from convective precipitation (Kida et al., 2009; Basist et al., 1998). Besides, screening method is also applied to conceptually categorize land types, such as snow cover, desert, etc Grody (1991); Sudradjat et al. (2011). The quality of rain rate retrieval algorithm with screening largely depends on the correct screening, which needs further investigation or offers large variations upon different observations.

1.2.3 Bayesian estimation methods

Modern algorithms to retrieve rainfall often rely on Bayes' theorem (Bayes and Price, 1763). Bayes' algorithm, which states that:

$$P(A|B) \propto P(A) \cdot P(B|A) \quad (1.3)$$

where A is the retrieved variable, e.g. rain rate; B is the observational variable, e.g. brightness temperatures from TMI; $P(A)$ is the prior probability distribution function (PDF) of retrieved variable A ; $P(B|A)$ is the PDF of the observational variable B conditioned on a specific value of A ; and $P(A|B)$ is the posterior PDF of A conditioned on a specific observational variable B .

Based on the Bayes' theorem, the prior PDF in Equation 1.3 is replaced by large data base rather than a continuous function in remote sensing retrievals (Chiu and Petty, 2006). The large data base for prior PDF collect candidate solutions with associated observed or modeled multichannel radiances. This variation of Baye's

theorem that involves the large data base for prior PDF was called a Bayesian Monte Carlo (BMC) method (L'Ecuyer and Stephens, 2002).

Among the recent work done for TRMM and GPM rain rate retrieval algorithm development, Bayesian estimation methods were majorly agreed upon (Evans et al., 1995; Kummerow et al., 1996; Olson et al., 1996; Haddad et al., 1997; Marzano et al., 1999; Bauer et al., 2001; Kummerow et al., 2001; Tassa et al., 2003; Di Michele et al., 2005; Grecu and Olson, 2006; Olson et al., 2006; Chiu and Petty, 2006; Seo et al., 2008; Petty, 2013). In Bayesian methods for microwave imager rain rate retrieval, a 'lookup' table is created from the training data. The 'lookup' table links the detectable variables to the retrieved variable. To retrieve rain rate, the detected variables are matched according to the 'lookup' table, and the rain rate is retrieved.

Bayesian methods were employed in one of the mainstream rain rate retrieval algorithms, Goddard Profiling Algorithm (GPROF) (Kummerow and Giglio, 1994b,a; Kummerow et al., 1996; Huffman and Coauthors, 1997; Kummerow and Coauthors, 2001; Wilheit et al., 2003; Shin and Kummerow, 2003; Masunaga and Kummerow, 2005; Kummerow et al., 2006; Kummerow, 1993; Kummerow et al., 2009). GPROF was mainly developed by Kummerow et al. (2001); Olson et al. (1996, 2006) over the ocean, and Ferraro et al. (1998); Ferraro and Li (2002) over land. The GPROF was firstly mentioned by Kummerow et al. (1996), and has undergone significant improvements. GPROF aims to retrieve instantaneous rainfall and the vertical structure of the rainfall. GPROF uses radiative transfer model and cloud resolving models (CRMs). GPROF 2004 was reported with representiveness errors (Kummerow et al., 2006) on representing light small rain system, since deep convective system is more interesting in CRMs. Besides, GPROF 2004 uses empirical screening routines developed for various sensors in its rain/no rain discrimination, and was reported by Kummerow et al. (2006) with incorrect ratio of stratiform, convective, and shallow

rainfall. Later on in GPROF 2010 constructed an a-priori database from observed TRMM radar and radiometer measurement. In GPROF 2010, CRM conservatively served to constrain parameters such as cloud water and ice that are not detected directly by PR. Compared with GPROF 2004, GPROF 2010 made the following progress over the ocean, which became the TRMM V7 product:

- No more rain screens;
- No more convective/stratiform separation; and
- Pixels are classified only by background sea surface temperature (SST) and total precipitable water (TPW).

GPROF 2010, compared with 2004, made the ocean part of the algorithm more consistent, although the land part is not changed much. However, some troublesome surfaces and coastlines remain problematic for light precipitation retrieval (Grody, 1991; McCollum and Ferraro, 2005; Sudradjat et al., 2011). It is crucial to find the way to optimize the noise-to-signal ratio, where the noise refers to any physical variation unrelated to rain rate and signal refers to variation due to precipitation.

UW algorithm was developed by Petty and Li (2013a,b) to retrieve the tropical rain rate, by reducing the dimensionality of the nine microwave channels to three pseudo-independent channels a.k.a. pseudo-channels, and applying Bayesian algorithm over the three pseudo-channels (Petty and Li, 2013a,b; Petty, 2013). Dimensionality reduction from nine microwave physical channels to three pseudo-channels greatly improved the efficiency of Bayesian estimation retrieving process (Petty, 2013). The dimensionality reduction would reduce the non-precipitating-related noise from TMI, maintain sample density, and significantly reduce the computational memory requirement.

As validation, improvement was shown when the UW algorithm was compared to 2A12 version 7 algorithm (Petty and Li, 2013a). In Figure 2-8 left, 2A12 v7 was

pointed out to have a slight overall positive bias of about 4% over ocean, while UW has no overall bias Petty and Li (2013a). Besides, the substantial smaller scatter in the UW was also shown in Figure 2-8 (Petty and Li, 2013a). In UW, the training data was made statistically identical to the retrieving data, completely independent from models or screening (Petty and Li, 2013a).

By Petty and Li (2013b), UW algorithm was compared with other prior published rain rate retrieving algorithms for TRMM. In the following are sum-ups of advantages of UW algorithm compared with other algorithms.

- The UW algorithm doesn't make conceptual distinction between land types (such as ocean and land). Rather, all surface distinctions are embodied in the particular transformation coefficients and a priori databases associated with each of seven surface classes.
- No 'screening' (rain/no-rain classification or stratiform/convective precipitation classification) is applied. Rather, the probability of non-zero rain is reflected through the posterior rain rate distribution generated by Bayesian algorithm.
- The result of rain rate retrieval is not just expected rain rates. Posterior distributions of rain rate are also provided.
- In the UW algorithm, TMI-PR matchup data were employed as the a-priori data base, and no cloud resolving models or simulated radiations are involved.
- The UW algorithm pre-averages the a priori database into a 5D lookup table, which consists of two environmental variables (surface skin temperature and total precipitable water content) and three reduced-dimensional pseudo-channels derived from nine microwave TMI physical channels (Petty, 2013).

- During the retrieval using UW algorithm, there is no weighting for candidate solutions.

Three pseudo-channels are derived using a two-stage principle component analysis (Petty, 2013), representing the three multichannel signatures most related to surface rain rate. Each of the three successive pseudo-channels in the Bayesian estimation algorithm serves to alter the posterior PDF of rain rate. It is rare that an algorithm produces an explicit posterior PDF of the retrieved variables. Therefore we have unique opportunity to rigorously evaluate the information content of successive pseudo-channels. Assuming other things we may examine whether three pseudo-channels are both necessary and reasonably sufficient to maximize the information from the 9 TMI channels.

1.3 Information Theory

As addressed by Kullback (1997), ‘speaking broadly, whenever we make statistical observations, or design and conduct statistical experiment, we seek information.’ Information theory is a mathematical subject that involves the rigorous quantification of information. The fundamental information theory was pioneered in the 1950s, mainly by Fisher (1956), Shannon (1956), and Wiener (1956).

The concept of Information entropy was first presented by Shannon (1948) to quantify the expected value of the information contained in a message. Therefore, the information entropy is hereafter called Shannon entropy.

1.3.1 Shannon Entropy

A detailed mathematical description of Shannon entropy is addressed in (Xu, 2006), both in discrete forms and continuous forms. The discrete Shannon entropy (DSE)

was written as:

$$DSE \equiv - \sum p_i \ln p_i \quad (1.4)$$

where p_i refers to the probability of occurrence of the i th possible outcome and $\sum p_i = 1$. The continuous Shannon entropy (CSE) is written as:

$$CSE \equiv - \int p(x) \ln p(x) dx \quad (1.5)$$

where $p(x)$ refers to a continuous PDF with variable x .

1.3.2 Relative Entropy

Assuming p and q are two PDFs, relative entropy is a non-symmetric measure of the difference between probability distributions p and q . Relative entropy is a measure with direction. Relative entropy from q to p , denoted as $RE(p||q)$, is a measure of the information lost when q is used to approximate p . Relative entropy from p to q , denoted as $RE(q||p)$, is a measure of the information lost when p is used to approximate q . $RE(p||q) \neq RE(q||p)$ (Kullbak and Leibler, 1951). Relative entropy has many synonyms in literatures, mean information for discrimination, Kullback-Leiber divergence, crowd entropy, information gain, information number, information divergence, KL distance, expected weight of evidence, discrimination (Verdu, 2010), etc.

Wald (1945) for the first time brought in the conception of ‘relative entropy’ to solve the sequential problem of testing. The literature described the relative entropy as the expected number of observations necessary for reaching a decision. Jeffreys (1945) further innovated the relative entropy with a symmetric expression. Despite the symmetry, the formula for relative entropy in (Jeffreys, 1945) turned out not quite useful in recent literature (Verdu, 2010). The innovated formula by Jeffreys (1945)

nowadays is addressed as separate kind of measure of relative entropy, called Jeffery's divergence (Verdu, 2010).

Kullbak and Leibler (1951) provided the first commonly accepted definition of relative entropy, which is the reason that relative entropy is sometimes called KL divergence. By Kullbak and Leibler (1951), relative entropy was called mean information for discrimination. The motivation to introduce the measure was to generalize the definition of information by Shannon (1956) and Viener (1956).

A detailed mathematical description of relative entropy is addressed by Xu (2006), both in discrete forms and continuous forms. The discrete Relative entropy (DRE) was written as:

$$DRE \equiv R(p, q) = \sum p_i \ln(p_i/q_i), \quad (1.6)$$

while the continuous form is

$$CRE(p, q) \equiv \int p(x) \ln[p(x)/q(x)] dx, \quad (1.7)$$

where p_i and q_i in Equation 1.6 are probabilities for a discrete distribution, and $p(x)$ and $q(x)$ in Equation 1.7 are PDFs for continuous distribution. In Bayesian statistics, $RE(p, q)$ is defined as a measure of the information gain in moving from a prior distribution q to a posterior distribution p (Chaloner and Verdinelli, 1995).

Information theory has been widely used in research in meteorology radar signal analysis (Xu, 2006), electrical signal analysis, and remote sensing area. In particular, within remote sensing area, Shannon entropy was employed by L'Ecuyer et al. (2005) and Cooper et al. (2005) to explore optimal MODIS channels for cloud property retrievals within the optimal estimation framework. In the present study, we evaluate the information content of the three successive pseudo-channels used in retrievals of rain rate from TMI, with both relative and Shannon entropies are employed.

1.4 Objectives

This paper has two major objectives:

- Investigate the physical meanings of the three successive pseudo-channels derived within the UW algorithm to retrieve surface rain rate over the ocean; and
- Quantify the information content of the three successive pseudo-channels in terms of altering the posterior surface rain rate distributions for each of several surface classes.

To achieve the objectives, the first two chapters are dedicated to the basic introductions on brightness temperatures and three successive pseudo-channels. The third chapter focuses on seeking the physical meanings of the three successive pseudo-channels, and describing the procedure of each pseudo-channels altering the rain rate probability distribution functions to retrieve rain rate. The fourth chapter focuses on quantifying the information content of three pseudo-channels from both necessary and sufficient perspectives. The last chapter is the conclusion.

Center Frequencies(GHz)	10.65	10.65	19.35	19.35	21.3	37.0	37.0	85.5	85.5
Polarization	V	H	V	H	V	V	H	V	H
Bandwidth (MHz)	100	100	500	500	200	2000	2000	3000	3000
Sensitivity (K)	0.63	0.54	0.50	0.47	0.71	0.36	0.31	0.52	0.93
IFOV (km x km)	63 x 37	63 x 37	30 x 18	30 x 18	23 x 18	16 x 9	16 x 9	7 x 5	7 x 5
Sampling Interval (km x km)	13.9x9.1	13.9x9.1	13.9x9.1	13.9x9.1	13.9x9.1	13.9x9.1	13.9x9.1	13.9x4.6	13.9x4.6
Integration Time (msec)	6.6	6.6	6.6	6.6	6.6	6.6	6.6	3.3	3.3
Main Beam Efficiency (%)	93	93	96	96	98	91	92	82	85
Beamwidth (half-power, degrees)	3.68	3.75	1.90	1.88	1.70	1.00	1.00	0.42	0.43

Figure 1-1: Data for postboost TMI sensors in various frequencies, including polarization (V is vertically polarized, H is horizontally polarized.), instantaneous field of view (IFOV), etc. (Kummerow, 2006)

Chapter 2

Passive Microwave Sensors and Rain Rate Retrieval

The nine passive microwave channels on TMI include dual polarization channels at 10 GHz, 19 GHz, 37 GHz, and 85 GHz, and a vertically polarized 23 GHz channel (Figure 1-1), which have varying responses to atmospheric constituents, such as water vapor, cloud and rain water, and ice particles aloft. Besides, the nine passive microwave radiants in TRMM have various degree of attenuation/scattering over various global surface features, such as water surface, desert, coastal regions, agricultural land, etc. The TRMM microwave imager (TMI) is responsible for passively measuring brightness temperatures of atmospheric constituents and the earth surface background. The associated precipitation radar (PR) is responsible for measuring the reflectivity due to rain drops. PR estimation of rain rate from reflectivity is based on Marshall-Palmer (Marshall and Palmer, 1948) drop-size distribution.

TMI covers a swath width of 833km, over three times as wide as the PR swath with a width of 247 km. Limited by swath width, PR often cannot fully provide the horizontal precipitation structure of mesoscale precipitating events. The precipitation data from PR overlaps with brightness temperatures by TMI over a limited swath at the center of TMI scans. Over two thirds of the TMI swath doesn't have direct access to the ground rainfall rate. Therefore, a precipitation algorithm is developed to link

the TMI brightness temperatures that relates clouds and hydrometeors to surface rain rate.

The reduced-dimensional Bayesian rain rate retrieve algorithm serves to predict what the PR would retrieve at those locations that are covered only by TMI without direct PR rain fall measurement. Besides, the rain rate retrieval can be extrapolated to satellites without PR but only microwave sensor. In the algorithm, nine TMI channels are reduced to three independent channels, which largely improves the computational efficiency and the robustness of the retrieval. Comparisons are shown to quantitatively demonstrate the improvement on retrieval quality.

2.1 Brightness Temperatures

2.1.1 Emission

By Planck's function, with a fixed wavelength, the intensity of radiation of this blackbody should be unique upon a given blackbody's temperature, and vice versa (Petty, 2006). Most real surfaces that emit less radiation at a given wavelength and temperature than the blackbody does according to Planck's function. The monochromatic emissivity ε_λ of a surface is defined as the ratio between the actual emitted radiation and the emitted radiation according to Planck's function ignoring other sources, for a fixed surface temperature T and wavelength.

$$\varepsilon_\lambda \equiv \frac{I_\lambda}{B_\lambda(T)}$$

where for a chosen wavelength λ , I_λ is the surface radiation, and the $B_\lambda(T)$ is the planck's function of a blackbody temperature T , which gives intensity of blackbody radiation. Conversely, one can convert intensity of monochromatic radiation from any surface to an equivalent blackbody temperature (a.k.a. Brightness temperature), using the inverse of Planck's function. According to the Rayleigh-Jeans Approximation,

Planck's function for microwave frequencies is a linear operator:

$$T_B \equiv B_\lambda^{-1}(I_\lambda) = B_\lambda^{-1}(\varepsilon \cdot B_\lambda(T)) = \varepsilon \cdot T$$

2.1.2 Transmittance

Assuming the absence of scattering or emission, for a given wave length λ , the radiation attenuation process through a optical path from point s_1 to s_2 can be calculated as

$$I_\lambda(s_2) = t(s_1, s_2) \cdot I_\lambda(s_1)$$

where $I_\lambda(s)$ refers to the intensity of radiation at point s , $t(s_1, s_2)$ is the transmittance of the constituent between s_1 and s_2 , that causes the radiation attenuation at the chosen wave length. The transmittance t can be calculated as:

$$t(s_1, s_2) \equiv \exp(-\tau(s_1, s_2))$$

where $\tau(s_1, s_2)$ is the optical thickness of the constituents from point s_1 to point s_2 (Petty, 2006).

2.1.3 Radiative Transfer Equations

When scattering of a constituents take place, the complete radiative transfer equation in differential form (Petty, 2006) is written as:

$$\frac{dI(\hat{\Omega})}{d\tau} = I(\hat{\Omega}) - (1 - \tilde{\omega})B - \frac{\tilde{\omega}}{4\pi} \int_{4\pi} p(\hat{\Omega}', \hat{\Omega}) I(\hat{\Omega}') d\omega' \quad (2.1)$$

where $\tilde{\omega} \equiv \beta_s/\beta_e$ is the single scattering albedo, β_s is the scattering coefficient and β_e extinction coefficient, B is the Planks' function, $d\tau$ is an increment of optical depth, $I(\hat{\Omega})$ is the intensity of radiation from a chosen direction represented by a unit vector $\hat{\Omega}$, $p(\hat{\Omega}', \hat{\Omega})$ is the scattering phase function for an arbitrary combination of incoming $\hat{\Omega}'$ and scattered directions $\hat{\Omega}$. On the right hand side of Equation 2.1, the first term

gives the attenuation, the second term gives the emission, and the last term gives the scattering source. The optical depth $d\tau$ can be calculated as:

$$d\tau = -k_e ds = -(k_e/\mu)dz$$

where k_e is the extinction coefficient. s is the geometric distance along an optical path of a constituent, which can be calculated with μ , the cosine value of zenith angle, and vertical coordinates in cloud remote sensing.

Equation 2.1 describes that the radiance along a particular line of sight (with optical depth of τ) either increase or decrease, depending on whether initial intensity of radiation $I(\hat{\Omega})$ is greater or less than emission $(1 - \tilde{\omega})B$ plus scattering $\frac{\tilde{\omega}}{4\pi} \int_{4\pi} p(\hat{\Omega}', \hat{\Omega})I(\hat{\Omega}')$. With assumption of non-scattering, a radiance passing through the atmospheric constituents would depend on the transmittance t and emission from constituents $B(T)$, as the first two terms in Equation 2.1 with $\tilde{\omega} = 0$. Incorporated with Rayleigh-Jeans approximation, non-scattering version of Equation 2.1 is written as:

$$dT_B = k_e(z)(T - T_B)dz/\mu \quad (2.2)$$

After Integrating Equation 2.2 from surface to the top of atmosphere, one can calculate the upward-directed atmospheric component of the brightness temperature T_B^\uparrow :

$$T_B^\uparrow = \frac{1}{\mu} \int_0^\infty T(z)k_e(z)t(z, \infty)dz \quad (2.3)$$

After integrating Equation 2.2 from top of atmosphere to surface, one can calculate the downward-directed atmospheric component of the brightness temperature T_B^\downarrow :

$$T_B^\downarrow = t(0, \infty)T_B^{toa} + \frac{1}{\mu} \int_0^\infty T(z)k_e(z)t(0, z)dz \quad (2.4)$$

Both T_B^\uparrow and T_B^\downarrow are atmospheric brightness temperatures towards the top of atmosphere and towards the surface of earth. The brightness temperature T_B observed

in the space by the satellite have direct relationship with T_B^\uparrow and T_B^\downarrow , and can be calculated as:

$$T_B = T_B^\uparrow + t(0, \infty)[\varepsilon_s T_s + (1 - \varepsilon_s) T_B^\downarrow] \quad (2.5)$$

When a radiance is received by the satellite microwave sensors, the signal consists of contributions from three parts about the earth (Figure 2-1): surface emission, atmospheric emission/scattering, and surface reflection.

The first part of radiation received by TMI comes from direct emission from the earth surface (gray dotted arrows in Figure 2-1). the emission depends on two major factors, the earth surface emission $\varepsilon_s T_s$ and atmospheric transmittance $t_A = t(0, \infty)$ in Equation 2.5.

The second part of radiation receive by TMI (blue solid arrows pointing upward in Figure 2-1) comes from upward emission of the atmospheric constituents T_B^\uparrow , a function of atmospheric temperature distribution $T(z)$, extinction coefficient $k_e(z)$, and transmittance $t(z, \infty)$ according to Equation 2.3.

The third part of radiation received by TMI is the radiance that originally are emission from atmospheric constituents to earth surface, get reflected by the earth surface, transmit through the atmospheric constituents for the second time, then reach sensor (blue downward arrows and green arrows in Figure 2-1). The third part of radiation that involves earth reflection depends on earth surface reflectivity $(1 - \varepsilon_s)$.

With scattering at presence, according to Equation 2.1, the emission $B(T)$ is reduced due to a increased $\tilde{\omega}$. Therefore in Equation 2.5, an increasing in scattering due to ice would reduce the upward atmosphere emission T_B^\uparrow and reflected emission T_B^\downarrow .

The ice particles can take in various forms, such as ice particles aloft in anvil or deep convective storms, and ice formed atmospheric hydrometeors (Petty, 1994a,b;

Bennartz and Petty, 2001). The ice particles in the clouds are strongly scattering, directly resulting in a reduced bulk emissivity of the cloud top (Bennartz and Petty, 2001).

There are other factors contributing to the brightness temperatures (Petty, 1994a) such as: the water vapor, reflected image of rain cell by the surface, FOV averaging process, etc.

2.1.4 Earth Surface Types

As the second term $t(0, \infty)\varepsilon_s T_s$ in radiative transfer equation (Equation 2.5), earth surface types provide background in TMI images for rain rate retrieval. Correctly assessing the surface type background would greatly aid the separation of atmospheric constituents (such as clouds, rain, snow, ice aloft etc) from the earth surface. It is known that in microwave sensors, surface background has a large variation in brightness temperatures. As an acknowledged challenge of microwave rain rate retrievals, some surface types also have reduced brightness temperatures from TMI as clouds, or precipitating events would, such as coastal regions, desert regions, and accumulated snow on the ground, etc. Therefore, it is extremely important to recognize the surface types from microwave sensor perspectives.

Observed by microwave remote sensors, earth surface is in general categorized into land, water, and sea ice (but sea ice is not a factor in the view of TMI). Land usually provides a warmer background in microwave brightness temperatures, than water (ocean, lake, etc) does (Figure 2-2). Ocean in TMI has large emissivity polarization difference compared with land (Figure 2-3), and provides a colder background than land (Figure 2-2).

Within land categories, various surface types are reflected in emissivities and surface temperatures under TRMM microwave channels. Over the land in TMI, veg-

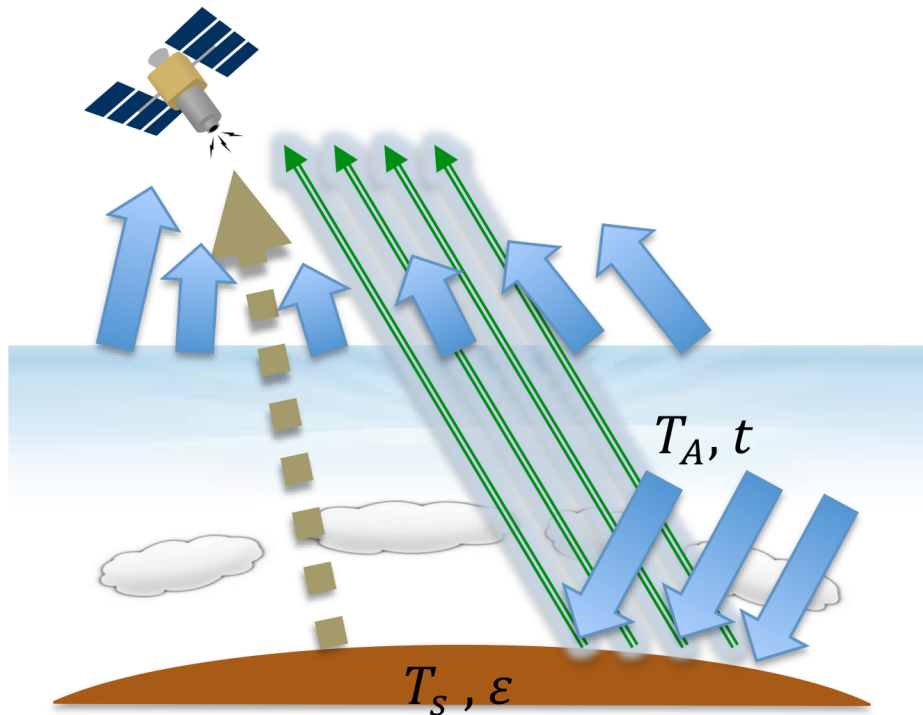


Figure 2-1: Passive microwave remote sensing mechanism. Green arrows are radiance reflected by the earth. Blue arrows are radiance emitted directly by the atmosphere. The gray dotted arrow represents radiance emitted directly from the earth surface. T_A is the averaged atmospheric temperature. T_s is the surface temperature. ϵ is the surface emissivity. t is the transmittance of the atmosphere.

etation area is observed to have large emissivities, but low emissivity polarization differences, compared with desert areas. Over at Tibetan plateau and some mountain areas, cold brightness temperature is shown on single channel map (Figure 2-4). Some surface types can not be easily shown through polarization difference or single channel, but can be distinguished through combinations of nine TMI channels.

In order to quantitatively categorize surface types, a more detailed algorithm was developed to categorize the surface types. This surface type division algorithm has a resolutions $1^\circ \times 1^\circ$, utilizing clustering technique applied to the means and covariances of TMI brightness temperatures for non-precipitating pixels (Petty and Li, 2013a).

As a result from the surface type algorithm, the surface is categorized into 6 classes as a background with warm and cold surface temperatures on each division Figure 2-5 by Petty and Li (2013a). The classes are named in Table 2.1. For each surface class except ocean (Class 0), there are cold and warm background difference denoted as ‘w’ and ‘c’ respectively.

In short, the surface backgrounds are reflected differently among nine TMI channels, and are categorized into six surface types. The categorized surface types serve as various background for the rain rate retrieval algorithm.

2.1.5 Cloud and Rain Water Emission and Ice Scattering

During a precipitating event, vertical structure of the event consists of the near surface hydrometeor (snow, rainfall, etc), the cloud and rain water, and the ice aloft. Cloud and rain water emission is considered to have important correlation with rain rate. In microwave remote sensing, the cloud water emission contributes to the received brightness temperatures (Equation 2.5). Therefore, measuring cloud and rain water emission by microwave channels in TMI would provide important information for rain rate retrieval.

Class	Description
0	Ocean
1	Vegetated land
2	Land/water mix (coast)
3	Desert
4	Rain forest
5	Tibetan Plateau and similar
6	Himalayan range and similar

Table 2.1: Surface type descriptions in Figure 2-5 (Petty and Li, 2013a)

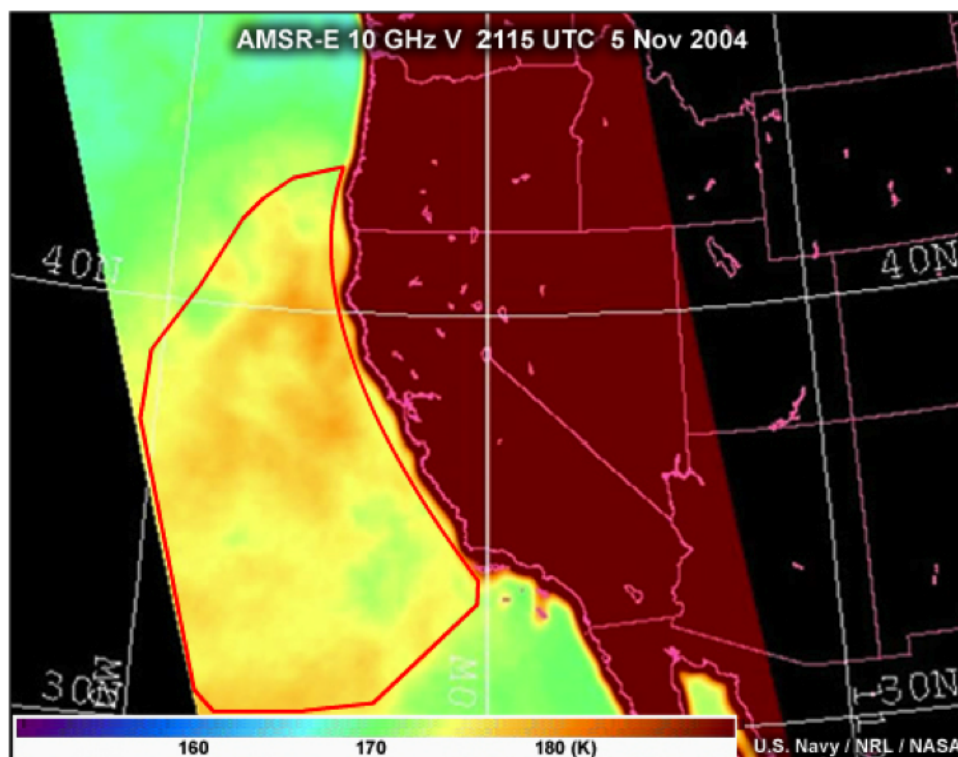


Figure 2-2: Land ocean brightness temperature difference reflected in the image of AMSR-E 10 GHz V on the west coast of US. (Courtesy to U.S.Navy/NRL/NASA)

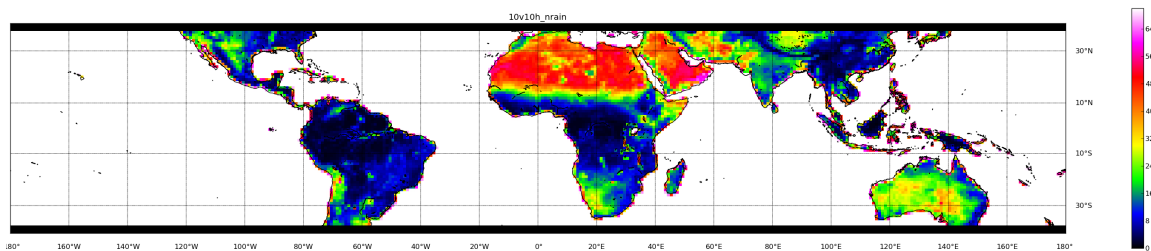


Figure 2-3: Map of brightness temperature differences, 10 GHz(V) - 10 GHz(H) for 2002 TMI non-precipitating pixels.

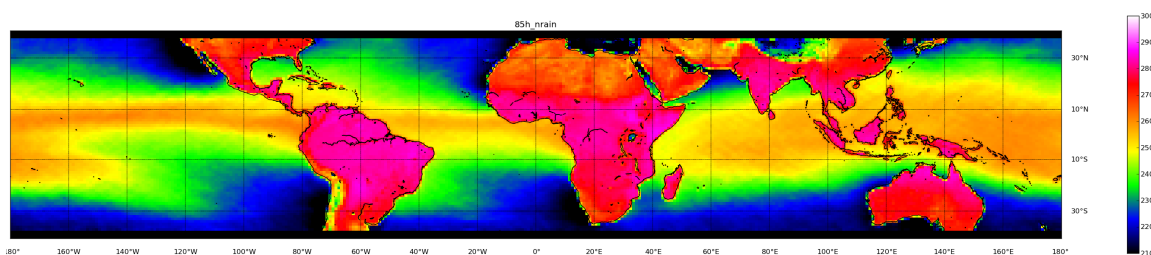


Figure 2-4: Map of brightness temperature of 85 GHz(H) for 2002 TMI non-precipitating pixels.

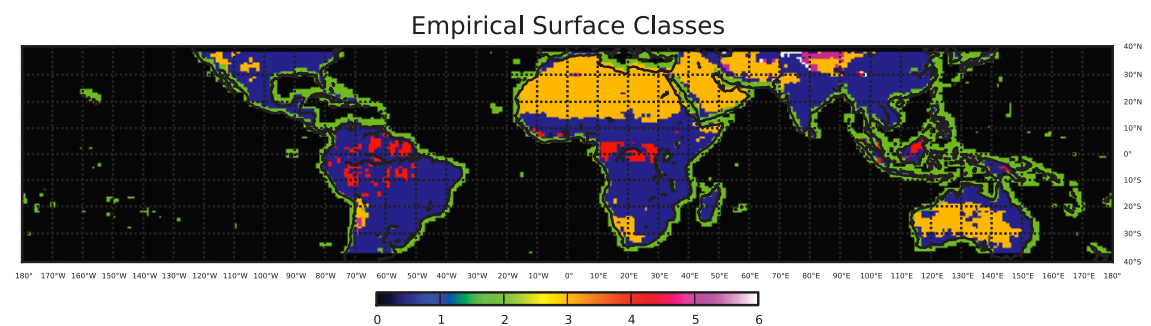


Figure 2-5: Map of the seven surface classes constructed by using TMI brightness temperatures for 2002. (Petty and Li, 2013a)

Besides, ice can be at presence, when there is severe convective storm, hurricanes, or anvil clouds. The ice aloft would be subject to scattering of radiance coming from the lower part of atmosphere. Therefore ice scattering is counted to be responsible to brightness temperature depression (Petty, 1994a, 2001). Therefore it is very important to investigate the nine microwave channel behaviors towards cloud and rain water emission and ice scattering. It is acknowledged that 10 GHz is less absorbed by cloud and rain water, more transparent to the precipitating clouds, and less sensitive to ice scattering than higher frequency channels. As frequency increases to 85 GHz, the TMI is more absorbed by cloud and rain water, reflecting more opaque atmosphere for precipitating events, and more sensitive to ice scattering (Petty, 2001).

An orbit of TMI and PR is chosen to reveal the relationship between PR measured rain rate and TMI channels (Figure 2-6). The ocean is used as a background. (The rest of this chapter, ocean is used as a background unless specially mentioned.) As is shown in Figure 2-6 left, the brightness temperature in 10 GHz and 19 GHz get warmer, when the rain rate is increasing. Typically, it is known that rain rate has a positive correlation with cloud and rain water. A high precipitating event usually is associated with thick cloud and rain water, which increase the emission from the cloud. It is known that ocean tends to provide a cold background ($160K \sim 200K$ for 10 GHz (V) and 19 GHz(V)), any cloud and rain water would obscure the ocean background and warm up the brightness temperatures.

Under 37 GHz and 85 GHz, the increase of rain rate is subject to an eventual decrease of brightness temperatures. The decrease in brightness temperature in 37 GHz and 85 GHz is believed to reflect the brightness temperature depression by ice scattering (Petty, 2001). When a rain rate increases to be $\geq 5\text{mm hr}^{-1}$, the ice may be very possible at presence which causes to decrease the brightness temperatures.

In short, it is confirmed in Figure 2-6 that lower frequency channels (10 GHz and

19 GHz) are very sensitive to cloud and rain water emission, while high frequency channels are very sensitive to ice scattering (37 GHz and 85 GHz).

2.1.6 Polarization and Rain Rate

The polarization in the microwave channels are not only playing a role in distinguishing earth surface backgrounds, but also are very important to reflect raining features.

As is known, ocean background provides cold TMI brightness temperature and is strongly polarized observed by TMI sensors. When a storm is detected over the ocean background, the optical thickness of the cloud and rain water would have a tendency to warm up the brightness temperature as the cold ocean background is obscured by the precipitating layer (Petty, 2001). The ice aloft (if ice is involved at all) would reduce the brightness temperature due to scattering, and also decrease the polarization. The vertical gradients of brightness temperatures in a storm ice particles aloft. The polarization of ice particles in TMI were addressed to depend on the orientation and size distribution of the ice particles.

Polarization is shown in TMI 1B11 data. In Figure 2-7, polarization is linked with rain rate over an orbit of TMI data. Figure 2-7 shows that when rain rate is small, typically, more radiation directly comes from the ocean, which appears to be strongly polarized and cold (black dots in Figure 2-7). As the rain rate increases, more and more ice aloft is involved, which is responsible for high frequency channels (85 GHz) to have brightness temperature depression (Figure 2-7 bottom, right). In short, high rain rate samples tends to have smaller polarization than low rain rate ones. Besides, high frequency channels are more sensitive to ice scattering than low frequency channels in TMI.

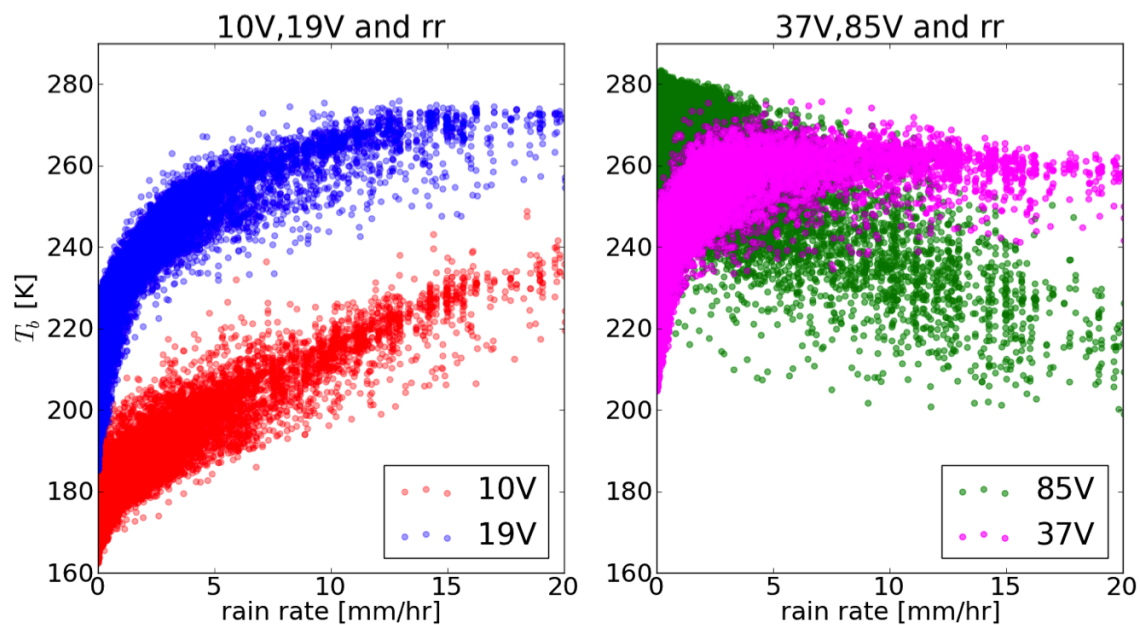


Figure 2-6: Typical response of different TRMM channels to rain rate. Red dots are 10 GHz. Blue dots are 19 GHz. Magenta dots are 37 GHz. Green dots are 85 GHz. The horizontal axis is retrieved rain rate, not directly measured PR rain rate. The plots here serve to illustratively show the trends of brightness temperatures. Using retrieved rain rate would have more samples that represent trends of TMI brightness temperatures.

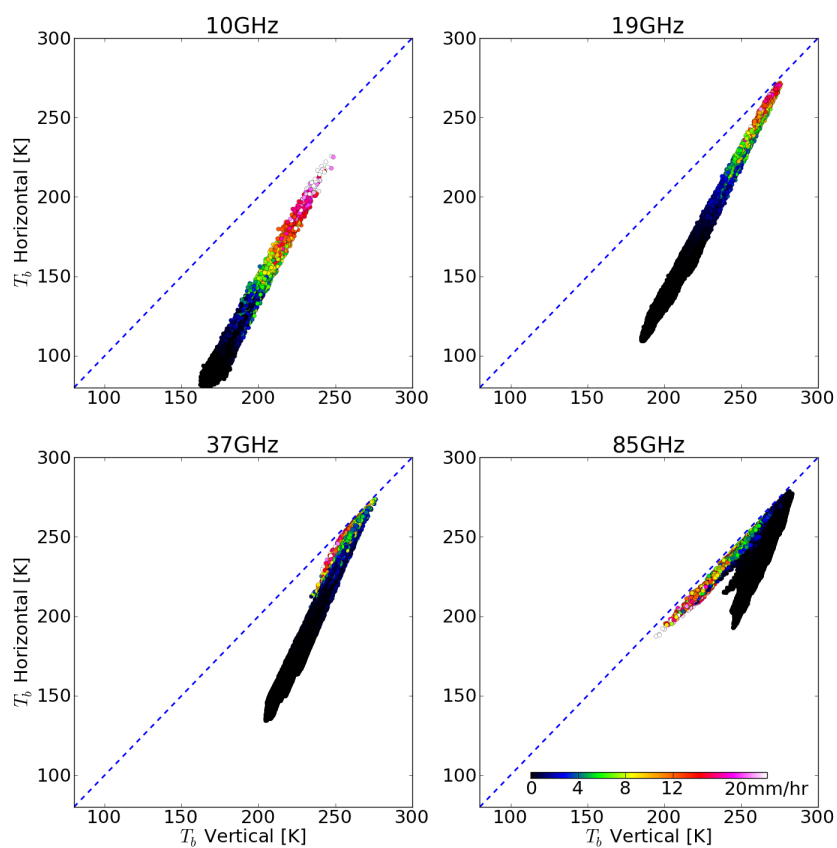


Figure 2-7: Scattering plots of polarizations with rain rate under TMI channel: (upper, left) 10 GHz, (upper, right) 19 GHz, (bottom, left) 37 GHz, (bottom, right) 85 GHz. Horizontal axes are brightness temperatures of vertically polarized channels, and vertical axes are brightness temperatures of horizontally polarized channels.

2.2 Bayesian Algorithm for Rain Rate Retrieval

To quantitatively retrieve the rain rate using the pre-mentioned features of each microwave channels, the reduced-dimensional Bayesian algorithm (also known as UW algorithm) was developed by Petty and Li (2013a). The goal for this algorithm is to take in the nine TMI channels and retrieve the surface rain rate at places where there is no PR available. The main idea of UW algorithm is to create a year long ‘look-up table’ that links the TMI brightness temperature to the PR rain rate, and retrieve rain rate. Compared with current GPROF (Kummerow et al., 2001), the reduced dimensional Bayesian algorithm features the high computational efficiency and availability of posterior PDF of rain rate (Petty and Li, 2013b,a).

As the first step, the dimension of variables are reduced. Often in times, the most dominant features (e.g. surface features) observed from microwave channels are not necessarily the desired features (e.g. rain and cloud related). Through the dimensional reduction, the geophysical noise is filtered out, and the sensitivity of precipitation related features is captured.

Thus, the dimensional reduction of nine microwave physical channels consists of two parts. The first part is to reduce the geophysical noises from physical channels. With only no-rain pixels, the variance due to the non precipitating features is converted to unit variance with zero cross-correlations (Petty, 2012). As a result, the geophysical noises due to surface types or other non-precipitating-related features are filtered out. The second part is to perform the second linear-transformation. When adding the pixels of precipitating events, all the information due to precipitation is collected. The principle component analysis is performed to collect the rain related information into smaller number of pseudo-channels.

The three modes from principle component analysis are independent ¹ from each other, thus are called independent channels (or ‘pseudo-channels’). During the process of dimensional reduction, much of the background noise is filtered out (Petty and Li, 2013b). In short, the dimensionality reduction serves to filter out the background noise, and reduce the number of channels from nine to three for Bayesian rain rate retrieval. In addition, each of the scene was tagged with surface skin temperature T_{skin} and total precipitable water (TPW) σ_{water} . Both T_{skin} and σ_{water} are inputs to the algorithm, obtained from the European Centre for Medium-range Weather Forecasting (ECMWF) Reanalysis ERA-Interim (Dee et al., 2011).

As the second step, the Bayesian ‘lookup table’ is created including two environmental variables (T_{skin} and σ_{water}) three independent channels (CH1, CH2, and CH3) and PR rain rate. The background noise is majorly filtered out when independent channels are generated, so the three independent channels can be used in the table with equal weights (Petty and Li, 2013b). Besides, to use the ‘lookup table’, the brightness temperatures for retrieval are required to be converted to the three independent channels.

As a result of the algorithm, posterior rain rate PDFs and related information are generated for all the gridded independent channels and environmental variables (column water vapor depth and surface temperature). The mean of each rain rate PDF is counted as the retrieved rain rate for each independent channel grid. Comparison between UW and 2A12 v7 was made (Petty and Li, 2013a) (Figure 2-8). The UW improves both precision of rain rate retrieval and efficiency of finding the match in the ‘lookup’ tables.

¹The three modes are independent in the linear sense. The higher order correlation between the three calculated modes (pseudo-channels) are possible to exist.

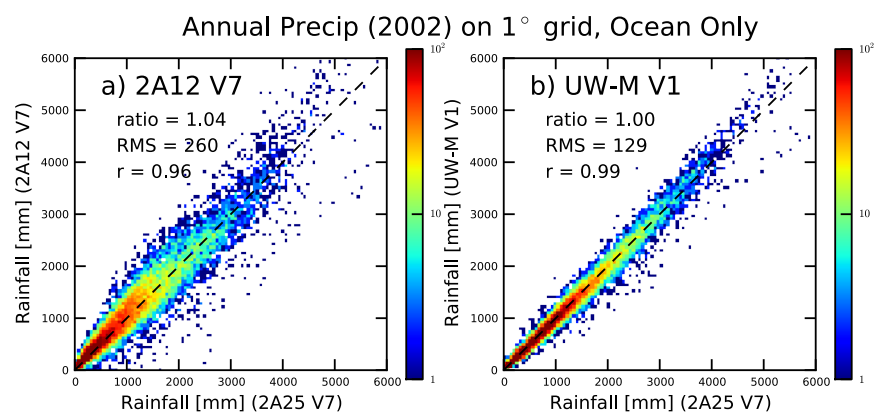


Figure 2-8: Comparisons of algorithms and PR rain rate data. (Left) comparison between PR rainfall rate and rainfall retrieved in 2A12; and (Right) comparison between PR rainfall rate and rainfall retrieved with UW algorithm. (Petty and Li, 2013a)

Chapter 3

Pseudo-channels

Pseudo-channels were developed from the nine TRMM microwave channels as the top three independent modes in the principle component analysis Petty and Li (2013a,b). To retrieve rain rate, the pseudo-channels were the middle product for finding the match in the trained ‘lookup’ table, representing nine TRMM microwave channels. However, the physical meaning of each pseudo-channels are not known, in order to fully corroborate the physical process of the UW algorithm. Gram-Schmidt process is employed to seek the essence of each pseudo-channel.

By producing pseudo-channels, the background noise such as land type, or other factors don’t necessarily reflect the rain rate features are filtered. More detailed algorithm of generating pseudo-channels were clearly addressed in Petty and Li (2013b,a); Petty (2013).

3.1 Over the Ocean

Precipitating features over the ocean can be relatively easier to recognized through microwave imagers than land. The ocean provides a colder and polarized background in the microwave channels than land. Relative to the ocean background, liquid water emission due to precipitating events appear to be warmer and unpolarized in microwave channels. Therefore, in lower frequency channels in microwave sensors, precipitating events tend to have a warm image over cold background (Figure 3-3

(a)). When ice aloft is involved, cold brightness temperature due to strong scattering and weak polarization are reflected in high frequency microwave channels (Figure 3-3 (b)).

It was addressed that the relationship between brightness temperatures and variations in different channels are nonlinear Petty and Li (2013b). To linearly decompose the 9 observed microwave channels to pseudo-channels, the observed channels are transformed into the following form Petty and Li (2013b):

$$x_{i,o} = \log(T_{\text{skin}} - T_{B,i}) \quad (3.1)$$

where, $T_{B,i}$ stands for brightness temperatures of different microwave channels, T_{skin} is the skin temperature of the surface. Through the transform (Equation 3.1), the nonlinearity and background noise are eliminated Petty and Li (2013b). Pseudo-channels over the ocean are generated with \vec{x} using principle component analysis.

3.1.1 Gram-Schmidt Process

Three pseudo-channels are calculated to be the key components to measure tropical rainfall rate over the ocean. ¹ Gram-Schmidt analysis is to convert three pseudo-channels to a set of observed channel vectors that are orthogonal to each other. In this way, the physical meaning of the pseudo-channels can be inferred from observed TMI channels. Besides, Gram-Schmidt analysis serves to filter out the dependence between pseudo-channels due to errors caused by manual division on pseudo-channel scatter plots (Figure 3-1). Therefore, the ‘distinct’ features of pseudo-channels can be achieved as a result.

¹It is worthwhile to notice that choosing the top three modes from the result of PCA is decided concerning trade of reduction in dimensionality from nine physical channels and rain rate retrieval algorithm quality. Further information regarding the number of kept modes for pseudo-channels is illustrated in Chapter 4 Information Theory.

The pseudo-channels are set to be zeros when there is no precipitating clouds at presence. CH1 ranges always positive, CH2 and CH3 can be positive and negative values. In the scatter plots of CH1, CH2, CH3 (Figure 3-1), fives cases are binned to further investigate each pseudo-channel (Table 3.1).

$$\vec{v}_i = \vec{T}_i - \vec{T}_0, i = 1, 2...5 \quad (3.2)$$

where \vec{T}_i refers to the vector of 9 microwave brightness temperatures in different cases with case number i , and \vec{v} is the vector of temperature difference of non-background cases subtracted by background vector. T_0 is the brightness temperature vector of background case (Table 3.1). The Gram-Schmidt analysis for pseudo-channels are calculate:

$$\vec{u}_1 = \vec{v}_1 \quad (3.3)$$

$$\vec{u}_2 = \vec{v}_2 - \text{proj}_{u_1}(\vec{v}_2) \quad (3.4)$$

$$\vec{u}_3 = \vec{v}_3 - \text{proj}_{u_1}(\vec{v}_3) \quad (3.5)$$

$$\vec{u}_4 = \vec{v}_4 - \text{proj}_{u_1}(\vec{v}_4) - \text{proj}_{u_2}(\vec{v}_4) - \text{proj}_{u_3}(\vec{v}_4) \quad (3.6)$$

$$\vec{u}_5 = \vec{v}_5 - \text{proj}_{u_1}(\vec{v}_5) - \text{proj}_{u_2}(\vec{v}_5) - \text{proj}_{u_3}(\vec{v}_5) \quad (3.7)$$

where \vec{u}_i refers to the of orthogonal vectors between three pseudo-channels. In another words, \vec{u}_1 (CH1 positive) is orthogonal to \vec{u}_2 (CH2 positive) and \vec{u}_3 (CH2 negative), but \vec{u}_2 and \vec{u}_3 are not orthogonal. similarly, two cases in CH3 are both orthogonal to CH1 and CH2 cases but are not necessarily orthogonal to each other.

Equation 3.2~3.7 provide the detailed procedure of calculating the orthogonal modes for different cases, which are plotted in Figure 3-2, demonstrating three pseudo-channel independent behaviors due to rain signal reflected on 9 observed microwave channels.

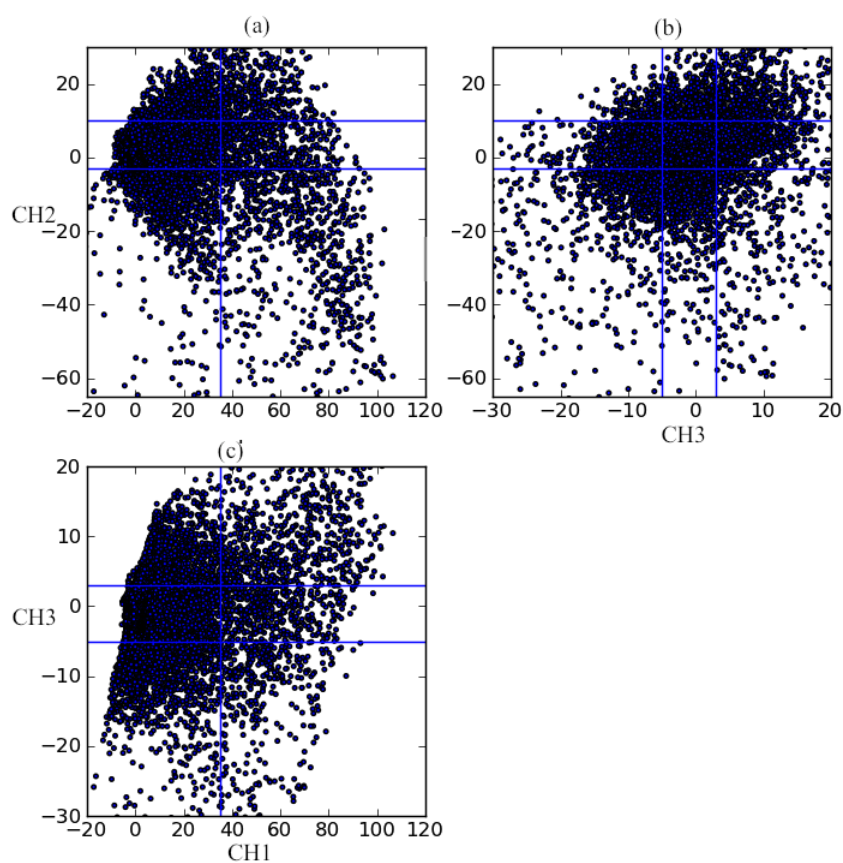


Figure 3-1: Scatter plots of three pseudo-channels over the ocean (1B11.20020911.27506.7.HDF): (a) CH1 and CH2, (b) CH3 and CH2, and (c) CH1 and CH3. The blue line refers to the division of different cases for Gram-Schmidt analysis

Case	Range	Description
0	$\text{CH1} < 35, 10 > \text{CH2} > -3, 3 > \text{CH3} > -5$	Background
1	$\text{CH1} > 35, 10 > \text{CH2} > -3, 3 > \text{CH3} > -5$	CH1 positive
2	$\text{CH1} < 35, \text{CH2} > 10, 3 > \text{CH3} > -5$	CH2 positive
3	$\text{CH1} < 35, \text{CH2} < -3, 3 > \text{CH3} > -5$	CH2 negative
4	$\text{CH1} < 35, 10 > \text{CH2} > -3, \text{CH3} > 3$	CH3 positive
5	$\text{CH1} < 35, 10 > \text{CH2} > -3, \text{CH3} < -5$	CH3 negative

Table 3.1: Case division for Gram-Schmidt analysis

3.1.2 CH1

In Figure 3-2 (a), the blue line gives the positive CH1 feature when CH2 and CH3 are close to zeros. Lower frequency microwave channels (10, 19, 37GHz) majorly contribute to positive CH1, while higher frequency channels (85GHz V and H) contribute little (Figure 3-2). It is known that lower frequency channels in TMI emphasize more on cloud liquid water emission from the precipitating clouds, while the high frequency channels have large contribution of ice scattering. Therefore, a positive CH1 independently describes the emission from cloud liquid water.

Shown in a storm (Figure 3-4 (a)) as an example, CH1 becomes positive at areas where 19GHz V shows warmer brightness temperature (19GHz V, in Figure 3-3 (a)). A warmer brightness temperature in 19GHz V reflects majorly emission from liquid precipitating cloud.

3.1.3 CH2

In Figure 3-2 (b), the black triangle curve refers to negative CH2 case reflected on 9 observed microwave channels by TMI. Figure 3-2 (b) shows insignificant contributions

by lower frequency channels, but rather high and positive contributions by higher frequency channels (85GHz V and H). 85GHz V and H feature in a combination of strong emission from cloud liquid water and high sensitivity to ice scattering. The negative CH2 case majorly reflects events with strong emission from liquid cloud and sensitive reaction toward ice scattering, such as strong convective precipitating events.

In Figure 3-2 (b), the green line is the positive CH2 case, when CH1 and CH3 are close to zeros. The positive CH2 case majorly reflects events that have lower frequency channels counted against high frequency channels. In a precipitating event, It is known that lower frequency channels majorly observes the emissions from cloud liquid water, and high frequency channels reflects both cloud liquid water and ice aloft. When high frequency channels are subtracted by lower frequency channels in a precipitating events, it is the ice aloft that is left. Therefore, a positive CH2 describes events that only have ice aloft, which can be anvil of the storm, or cirrus clouds.

Shown in a storm (Figure 3-4 (b)) as an example, CH2 becomes negative at areas where 85GHz V (Figure 3-3 (b)) shows colder brightness temperature, which reflects strong ice scattering. The ice aloft overlaps with areas with strong emission between 19GHz V and 85GHz V (Figure 3-3 (a) and (b)), which indicates the ice aloft is part of the deep convective system. In Figure 3-4 (b), CH2 appears positive at areas surrounding deep convective rain bands (Figure 3-3 (c) and 3-4 (d)). The area where CH2 appears positive corresponds with very little rain rate. The anvil of the convective system is known to have thin ice aloft but doesn't usually precipitate. Therefore positive CH2 indicates majorly the anvil of the convective system.

3.1.4 CH3

In Figure 3-2 (c), the red line and magenta lines are negative and positive CH3 cases receptively. Both red and magenta curves (Figure 3-2 (c)) are quite symmetric at axis

$y = 0$ line, with sinusoid shapes, which resemble the higher order mode in Fourier series. In Figure 3-4 (c), strong positive and negative CH3 areas are coupled together, located at areas with strong horizontal rain rate gradient. At areas with very little horizontal precipitation gradient, there is little variation of CH3. It is inferred that CH3 plays a role as ‘edge detector’ of precipitating events, although further research is needed to analyze the dipole structures of CH3 to seek its association with scanning geometry of TMI.

The 9 observed microwave channels are known to have different of field of views (FOVs). The different size of FOVs among microwave channels may cover different fractures of non precipitating and precipitating areas over the sharp horizontal rain rate gradient, though all the FOVs are centered at same pixels. CH3 may captures the brightness temperature variations of nine microwave channels due to brightness temperatures averaged in different FOVs. The CH3 concerning different FOVs would be especially sensitive when the horizontal rain rate gradient is large.

3.2 Probability Distribution Functions

The ‘lookup’ table has five dimensions, which are skin temperature, total precipitable water (TPW), and three pseudo-channels. With in each line of the ‘lookup’ table, the samples with different rain rates are binned to form a distribution. The retrieved rain rate within each line of the ‘lookup’ table is calculated as the mean of the distribution.

It was addressed that the skins temperature, TPW, and three pseudo-channels need to be binned in an appropriate bin sizes, so that the samples in each bins are sufficiently densely populated but not too large Petty and Li (2013b). It was also realized that pseudo-channels range from 10^1 to 10^2 , yet most of the samples are distributed around 10^1 , and very few get to 10^2 or higher Petty and Li (2013b).

Therefore, a scheme is used to convert the pseudo-channels for bin division.

$$Y_i \equiv \Delta \arctan\left(\frac{PCH_i}{\Delta}\right) \quad (3.8)$$

where, PCH_i refers to pseudo-channel values ($i = 1, 2, 3$), $\Delta = 15$ for pseudo-channels. Similar conversion is applied to T_{skin} with $\Delta = 5K$ and TPW with $\Delta = 10mm$. From here on in statistic analysis, the pseudo-channels, skin temperatures and TPWs take on the converted binned values, not original values, unless statement specifies.

Probability distribution functions are generated, with rain rate binned exponentially in mm hr^{-1} :

$$[0.0, 0.01, 0.02, 0.03, 0.05, 0.1, 0.2, 0.3, 0.5, 1.0, 1.7, 3.0, 5.2, 10.0, 17.0, 30.0]$$

where, 0.0 has its own bin, and the rest goes from $0 < R \leq 0.01$ and so on. When none of the three pseudo-channels are involved in the retrieval, the probability distributions of rain rate only vary with the two environmental variables (a.k.a. T_{skin} and TPW), which are considered distributions of climatological data (Figure 4-3, 4-4, and 4-5 (a)). As each pseudo-channel is added to the ‘lookup’ table, the probability distributions are altered, and retrieved rain rate becomes closer to the real value (Figure 4-3, 4-4, and 4-5 (b)(c)(d)). The three pseudo-channels are adding information into the rain rate retrieval process. It is very important to understand how much information each pseudo-channel provides to rain rate retrieval, which is discussed further in the next chapter.

In short, Gram-Schmidt analysis revealed the independent features each pseudo-channel describes over the ocean. CH1 describes the emission of cloud and rain water. CH2 describes the ice aloft, with negative CH2 for ice on top of convective systems and positive CH2 for ice aloft as anvils. CH3 is the ‘edge detector’, measuring the

horizontal rain rate gradient. However, it is still unknown about how important each pseudo channel is to retrieve rain rate. The significance of each pseudo-channel for retrieving rain rate includes how important are the pseudo-channels between each other and are three pseudo-channels enough to retrieve rain rate, and whether the 'forth' (or higher) pseudo-channels are necessary for the purpose of improving the rain rate retrieval precision.

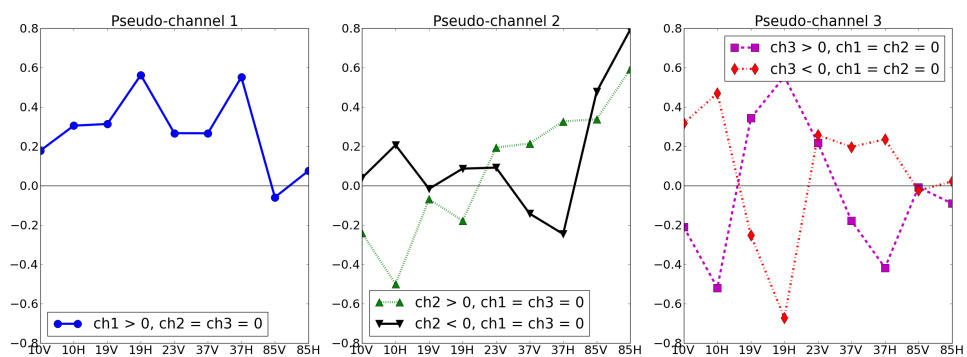


Figure 3-2: Orthogonal modes of 9-microwave-channel distributions with: CH1 positive in blue dotted line, CH2 positive in green triangles, CH2 negative in black triangles, CH3 positive in magenta squares, and CH3 negative in red diamond.

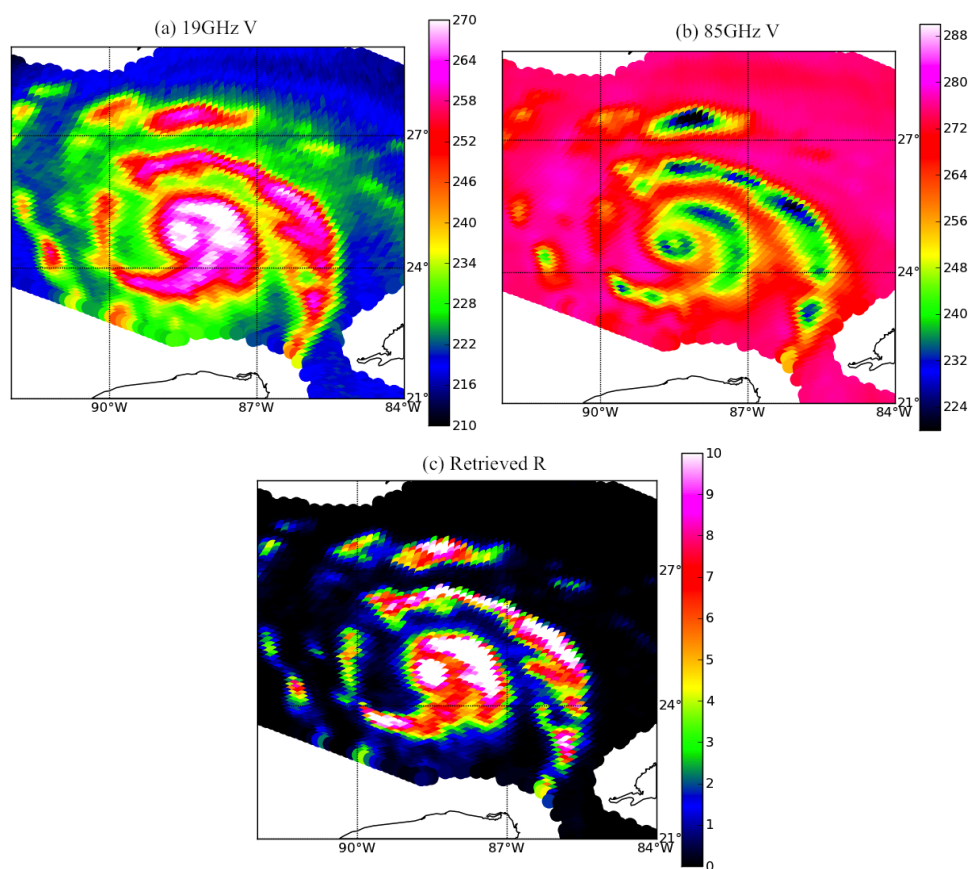


Figure 3-3: Microwave channels 19GHz V, 85GHz V, and retrieve rain rate of Hurricane Lily in October 2002, to the southwest of Florida. (a) 19GHz V brightness temperature (K), (b) 85GHz V brightness temperature (K), and (c) retrieved rain rate in mm/hr.

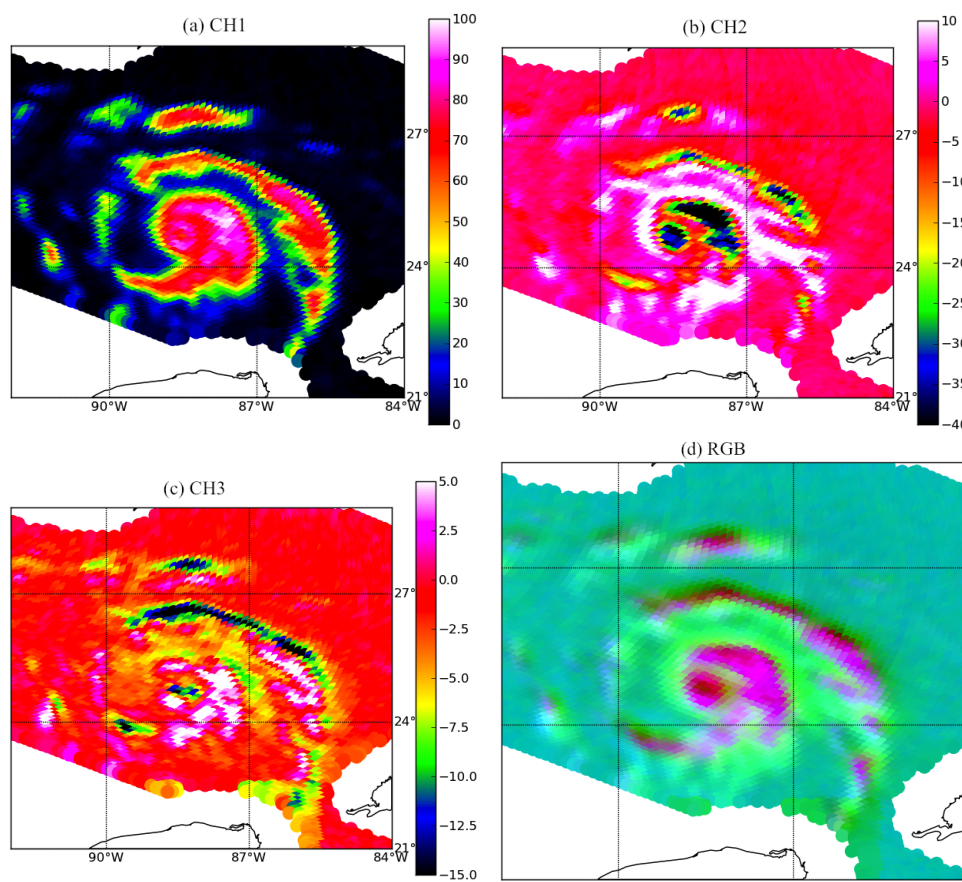


Figure 3-4: Pseudo-channels of Hurricane Lily in October 2022, to the southwest of Florida. (a) CH1, (b) CH2, (c) CH3, and (d) RGB plot of CH1 (red), CH2 (green), and CH3 (blue).

Chapter 4

Information Theory

In previous chapters, the physical insight of three pseudo-channels are analyzed. It was observed that CH1 is related to column rain water, CH2 is related to ice scattering aloft, and CH3 responds to edges and gradients of horizontal precipitation distribution. Besides, posterior probability densities are calculated based on one, two, or three pseudo-channels. The posterior PDFs based on one, two, or three pseudo-channels allow us to quantitatively evaluate the information added by each successive channel.

Both Shannon entropy (SE) and relative entropy (RE) are employed to evaluate the information that is added by three successive pseudo-channels to the rain rate retrieval.

4.1 Shannon Entropy and Relative Entropy

In this section, both SE and RE are calculated in the toy models to reveal their distinctions in quantifying the information content.

4.1.1 Gaussian Distribution

A Gaussian distribution $f(x)$ is designed to represent the prior distribution.

$$f(x) = \frac{1}{\sigma\sqrt{2\pi}} \exp -\frac{(x - \mu)^2}{2\sigma^2} \quad (4.1)$$

where $\sigma = 2.0$ is the standard deviation, $\mu = 0.0$ is the mean. The bins are unevenly divided from -10 to 10 , with exponentially divided spacing. The posterior distribution $g(x)$ is designed to be Gaussian distribution with signal or dispersion change. When signal is changed, the mean of Gaussian is shifted as: $\mu = -4.0, 0, 4.0$. When the dispersion is changed, the standard deviation varies as $\sigma = 1.0, 2.0, 4.0$. The content of information that changes distribution from f to g is evaluated for each bins in terms of Shannon entropy change and relative entropy change. According to Equation 1.6 and 1.7, the relative entropies for both discrete and continuous forms have identical results. Therefore, relative entropy $RE(f \rightarrow g)$, Discrete Shannon entropy difference $\Delta DSE(f \rightarrow g)$, and Continuous Shannon Entropy difference $\Delta CSE(f \rightarrow g)$ are calculated for each bins, and the results for signal or dispersion variations are shown in Figure 4-1. In Figure 4-1, the blue shaded distribution in the upper panel refers to the prior distribution $f(x)$ and the pink shaded distribution refers to the posterior distribution $g(x)$.

In Figure 4-1(a), $f(x)$ and $g(x)$ are overlapping with each other, which indicates no information is provided to change the distribution, and $RE = \Delta DSE = \Delta CSE = 0.0$.

Relative Entropy In Figure 4-1 (b) and (c), signal is shifted to the right and left respectively to same distance. The RE s are shown the same for signal shiftings to both directions. It is noticed that RE has a large positive contribution at bins where the prior probability is close to 0 (for example, less than 0.02), but the posterior probability is large (for example above 0.15) in Figure 4-1 (b) or (c). RE has a very small and negative contribution at bins where the prior probability is large (for example, above 0.15), but the posterior probability is close to 0 (for example, less than 0.02) in Figure 4-1 (b) or (c).

In Figure 4-1 (d) and (f), the RE values are small compared with RE in Figure 4-1 (e). It is noticed that the signals in Figure 4-1 (d)–(f) are not shifted, only the dispersions are changed. In Figure 4-1 (e), the dispersion is flattened, when less possible area becomes more possible at the skew part, and more possible area becomes less possible at the peak part. RE in Figure 4-1 (e) is largely contributed by the increase in possibility at the skew parts. It is noticed that upon all the cases, RE become more positive at places where it is not quite possible in the prior distribution but it becomes very possible in the posterior distribution. This process that greatly improves the probability from a case not likely to happen at all to a case that quite likely to happen can also be described in the real life as surprise. Therefore, it is confirmed that RE measures the signal shift through a piece of information. In another word, RE quantifies the ‘surprise’ that a piece of information is adding to change the prior distribution.

Shannon Entropy In Figure 4-1 (b) and (c), the signal shifts change very little on Shannon Entropy, $\Delta CSE = 0.0$ and $\Delta DSE = -0.28, 0.34$ (-0.28 to the right and 0.34 to the left respectively). The spacing for bin division is uneven in Figure 4-1.

According to Equation 1.4 and 1.5, both DSE and CSE are identical when bins are evenly divided for PDFs. The Gaussian distribution experiment with undivided bins are designed to examine the difference between ΔDSE and ΔCSE . In Bayesian statistics, $\Delta DSE(f \rightarrow g)$ and $\Delta CSE(f \rightarrow g)$ are quantities to measure the information content of the message that changes prior PDF f to posterior g . It was addressed that DSE is uniquely defined by the probability measure over the message, not dependent on bin sizes. And CSE measures the message with probability density (involving both probability and bin division) (Frigg and Werndl, 2011). By definition, DSE is uniquely defined for a discrete probability message (such as flipping the

coins), not dependent on the bin sizes. CSE is uniquely defined for a continuous probability density message (PDFs) not dependent on the bin sizes.

In short, to describe information content of PDFs, the CSE and DSE would be identical if the bins are evenly divided. Otherwise CSE for quantifying the information measure PDFs would include the coordinates influence. This conclusion is also confirmed by the numerical experiment involving Gaussian distribution.

According to Equation 1.4, ΔDSE counts each bin equally in significance over the Gaussian PDFs (for example the Gaussian PDF $f(x)$ in blue shades). Yet in the experiment the Gaussian PDFs have unevenly divided bins. Therefore calculated ΔDSE is a combination of information content of the PDF message and the bin coordinates that is chosen to describe the message. The signal shift to the left and to the right in Figure 4-1 (b) and (c) are quantified by ΔDSE differently when the bins are not evenly divided. It is observed that Shannon entropy (ΔCSE) doesn't change when there is a signal shift (Figure 4-1 (b) and (c)).

When the bins are evenly divided in 4-2 (a) and (b), ΔDSE counts each bin with equal significance. The calculated ΔDSE , under evenly divided bins, is able to exclusively quantify the Shannon entropy information content solely due to signal shift, without the influence of binning. As shown in 4-2, signal shifts on both positive and negative side of the axis correspond with zero change in ΔDSE , but a same RE measure. As comparison, for same Gaussian function signal shift, ΔCSE correctly measures the information content regardless of bin division (4-1 (b) and (c)). ΔCSE has limitations, compared with ΔDSE . ΔCSE is used for continuous distributions. When used in discretized fashion, ΔCSE becomes invalid when bin width is zero (Equation 1.5).

The posterior data for three successive pseudo-channels is made into discrete cumulative distributions, with unevenly discretized binning. According to the distribu-

tion, more samples are falling into the lower or zero rain rate range than high rain rate range. Thus, the bins for rain rate is set exponentially so that narrower bins at lower end (for example, $0.1 \sim 0.2 \text{ mm hr}^{-1}$) is equally important as wider bins at higher end (for example, $10 \sim 20 \text{ mm hr}^{-1}$). Besides, the first bin is non-raining bin, which is counted as bin with zero bin width. Due to the discrete form and the non-raining bin, ΔDSE is more suitable than ΔCSE to take measurements for Shannon entropy of three successive pseudo-channels.

A couple of reversed processes for PDF change in dispersion are depicted in Figure 4-1 (e) and (f). Figure 4-1 (e) shows the less dispersion in blue turning to more dispersion in pink. Figure 4-1 (f) shows the opposite. It is reflected in entropy distribution that equal and opposite Shannon entropies changes (ΔCSE and ΔDSE) are shown for 4-1 (e) and (f). When the posterior PDF becomes more spread out (flattened in PDF curve shape), ΔDSE and ΔCSE are positive. When the posterior PDF becomes less spread out (sharpened in PDF curve shape) ΔDSE and ΔCSE are negative. In short, the Shannon entropies measure exclusively the dispersion change of a distribution, and cannot reflect the signal change at all.

4.2 Pseudo-channels

The rain rate probability distribution are generated for retrievals with one, two, or three pseudo-channels. The raining samples are observed to be more clustered at the lower rain rate range. Much fewer samples falls into higher rain rate range more scattered than lower rain rate samples. The rain rate samples are observed to be distributed in an exponential fashion. In another words, light rain appears to be much more likely than heavier rain. Therefore, bins are designed to be in exponential, where, for example, rain rate bin ranging from 0.01 to 0.02 mm hr^{-1} is considered as

important as the bin from 10 to 20mm hr⁻¹ in the information content analysis.

The discrete Shannon entropy difference and relative entropy are calculated to measure the information content of each pseudo channels to the rain rate retrieval. Three cases are picked out to demonstrate the probability distribution changes by adding three successive pseudo-channels in Figure 4-3, 4-4, and 4-5.

In Figure 4-3(a), the probability distribution is based on rain rate samples collected according to the environmental variables (skin temperature and total precipitable water ¹). When CH1 is added (CH1 = 41 in Figure 4-3(b)), the posterior probability distribution has a signal shift, which is reflected by positive *RE*. *RE* = 2.26 in Figure 4-3(b) is bigger than *RE* = 1.03 in (c) and *RE* = 0.01 in (d). Clearly reflected by *RE*, the signal change between prior and posterior distributions by adding CH1 in Figure 4-3 (a) and (b) is more significant than shifts by adding CH2 or CH3 in this presented case. It is worthwhile to notice that CH1 CH2 and CH3 are added in order to test their information contributions to rain retrieval. The information contributions of these three successive pseudo-channels depend on the order that they are added successively during the retrieving process and their own independent information contents. In this chapter of information theory, our focus is mainly on evaluating within a set order (i.e. CH1, CH2, and then CH3), how much information each pseudo-channel is adding to the retrieval in addition to the priorly added channels and environmental variables. For example, CH3's information content in our information analysis refers to how much additional information CH3 contributes more than environmental variables, CH1, and CH2. It is noticed that in climate data Figure 4-3 (a), zero rain rate bin has the largest amount of samples. The dispersion change between Figure 4-3 (a) and (b) are not large compared with Figure 4-3 (b) and (c), which is reflected by

¹All the values of T_{skin} , σ_{water} , CH1, CH2, CH3 in the Information theory chapter are all scaled values for statistical purposes, not the physical values. The scaling process is mentioned in Petty and Li (2013a).

$\Delta SE = -0.12$ in (b), much smaller than $\Delta SE = -0.92$ in (c). In short, ΔSE and RE reflect that adding CH1 in Figure 4-3 brings significant signal change of rain rate probability distribution, but not strong dispersion change, compared with adding CH2.

Between 4-3 (b) and (c), the signal shift between prior and posterior distributions is not large compared with (a) and (b), which is reflected by RE value. $RE = 1.03$ for adding CH2 in Figure 4-3 (c) is only half of $RE = 2.26$ for adding CH1 in Figure 4-3 (b). The dispersion is eliminated by adding CH2 from Figure 4-3 (b) to (c). It is observed that Figure 4-3 (b) has a wider dispersion than (c), which is reflected by negative ΔSE value in (c), greater in magnitude than $\Delta SE = -0.12$ in Figure 4-3 (b). In short in Figure 4-3 (c), the RE shows that adding CH2 brings about a signal shift on rain rate probability distribution, not as much as adding CH1 in (b). Besides, in Figure 4-3 (c), ΔSE shows that adding CH2 decreases dispersion on posterior rain rate probability distribution, more than adding CH1 does in (b).

Between Figure 4-3(c) and (d) probability dispersion, the signal shift between prior and posterior distributions is very little, so is the dispersion change. $\Delta SE = -0.04$ and $RE = 0.01$ in Figure 4-3(d) are much closer to zero than those in (b) and (c). In short, CH3 in 4-3(d) adds little information to the probability distribution change, compared with CH1 or CH2. As a summary for Figure 4-3, CH1 brings significant signal change of rain rate probability distribution, compared with CH2 and CH3. In another word, CH1 in Figure 4-3 provides majority of information content for rain rate retrieval algorithm compared with CH2 and CH3.

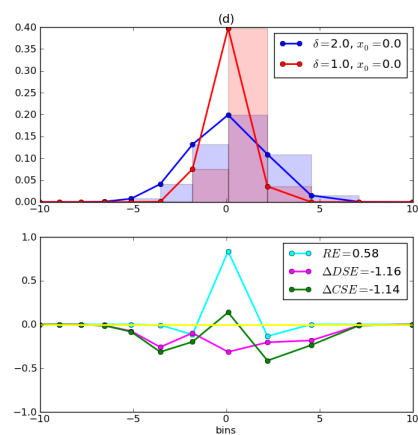
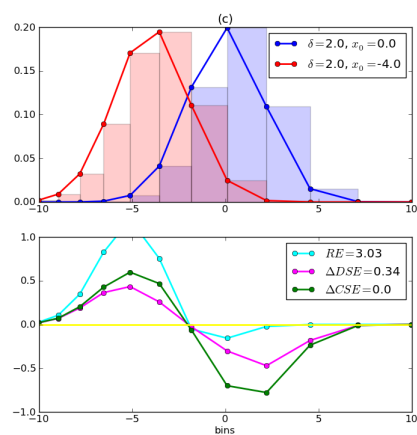
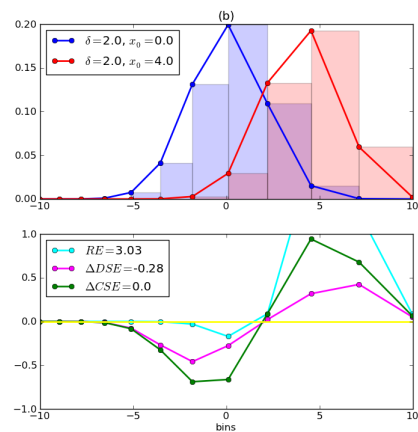
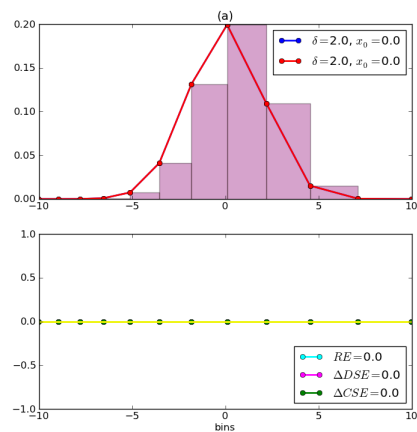
In Figure 4-4, another set of rain rate probability distributions are shown to demonstrate the information contents provided by three successive pseudo-channels. In Figure 4-4(b), little is changed in the probability distribution signal shifting by adding CH1, which is reflected by small value $RE = 0.03$ (small compared with

$RE = 2.1$ in Figure 4-4(c)). In Figure 4-4(c), the zero rain rate bin sample number is reduced, and numbers of samples in bins with intermediate/light rain rate $0.05 \sim 1.0\text{mm/hr}$ are increased by adding CH2. In correspondence, $RE = 2.1$ reflects the distribution signal in Figure 4-4c is shifted towards the light rain rate bins relative to (b), and $\Delta SE = 2.37$ reflects the dispersion of the probability distribution in (c) is increased relative to (b). From Figure 4-4(c) to (d), the distribution changes very little, which is reflected by small RE and ΔSE in (d) compared to those in (c). In short, CH2 in Figure 4-4 contribute majorly to the rain rate distribution, by providing the largest information content RE of all three successive pseudo-channels.

In Figure 4-5, another set of rain rate probability distributions are shown to demonstrate the information contents provided by three successive pseudo-channels. In Figure 4-5 (a), (b), and (c), small RE and ΔSE compared with those in (d) reflect small information contents CH1 and CH2 provide for rain rate retrieval in this specific case. In Figure 4-5(d), $RE = 1.81$ reflects significantly large signal shift of rain rate distribution when CH3 is added. In Figure 4-5(d), $\Delta SE = 2.3$ reflects significantly large dispersion of rain rate distribution when CH3 is added. From the rain rate probability distribution in Figure 4-5, probability of intermediate/light rain rate ($0.05 \sim 1.0\text{mm/hr}$) is increased and zero rain rate probability is decreased when CH3 is added. In short, CH3 in case demonstrated by Figure 4-5 has major influence on rain rate retrieval, by having the largest information content of all three pseudo-channels.

As a sum-up, three over-ocean cases in correspondence of Figure 4-3, 4-4, and 4-5 are chosen to confirm the physical indication of RE and ΔSE . Based on the analysis in this section, three successive pseudo-channels can all provide large information content, altering the posterior rain rate probability distributions in the Bayesian algorithm.

However, the information content of three successive pseudo-channels over other land types are still unknown. Also, it is unknown of how much keeping first one, two or three pseudo-channels would alter the rain rate retrieval results. Moreover, it is important to understand what ranges of retrieved rain rate are influenced most by each pseudo-channels. Are higher order pseudo-channels (ex, CH2, CH3) always necessary to keep to retrieve rain rates of all samples? Is the higher order pseudo-channel (ex, CH4, CH5, etc) necessary to increase the precision of the presented Bayesian algorithm? Further analysis is performed in the next section to associate pseudo-channels with retrieved rain rate over each surface type, using RE and ΔSE to quantify the rain rate distribution change.



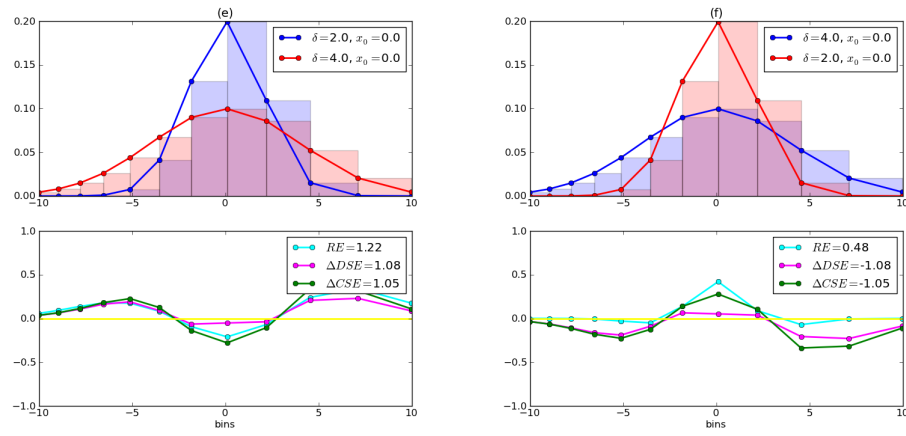


Figure 4-1: Information entropy changes between two Gaussian distributions over unevenly divided bins. Blue blocks are normal distribution before, and pink blocks are normal distribution afterwards. All upper panels are probability density functions (PDFs), and lower panels are changes of informational entropy of different kinds. The green lines are continuous Shannon entropy difference (ΔCSE). The magenta lines are discrete Shannon entropy difference (ΔDSE). The cyan lines are relative entropy (RE).

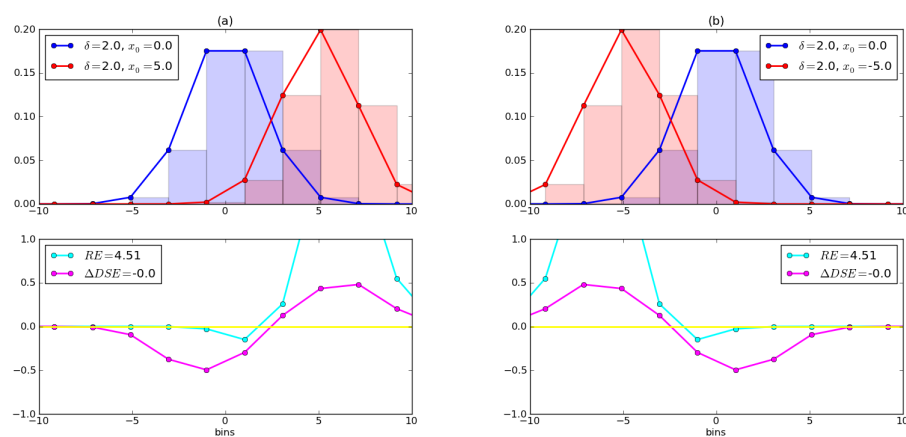


Figure 4-2: Information entropy changes between two Gaussian distributions over evenly divided bins. Blue blocks are normal distribution before, and pink blocks are normal distribution afterwards. All upper panels are probability density functions (PDFs), and lower panels are changes of informational entropy of different kinds. The magenta lines are discrete Shannon entropy difference (ΔDSE). The cyan lines are relative entropy (RE).

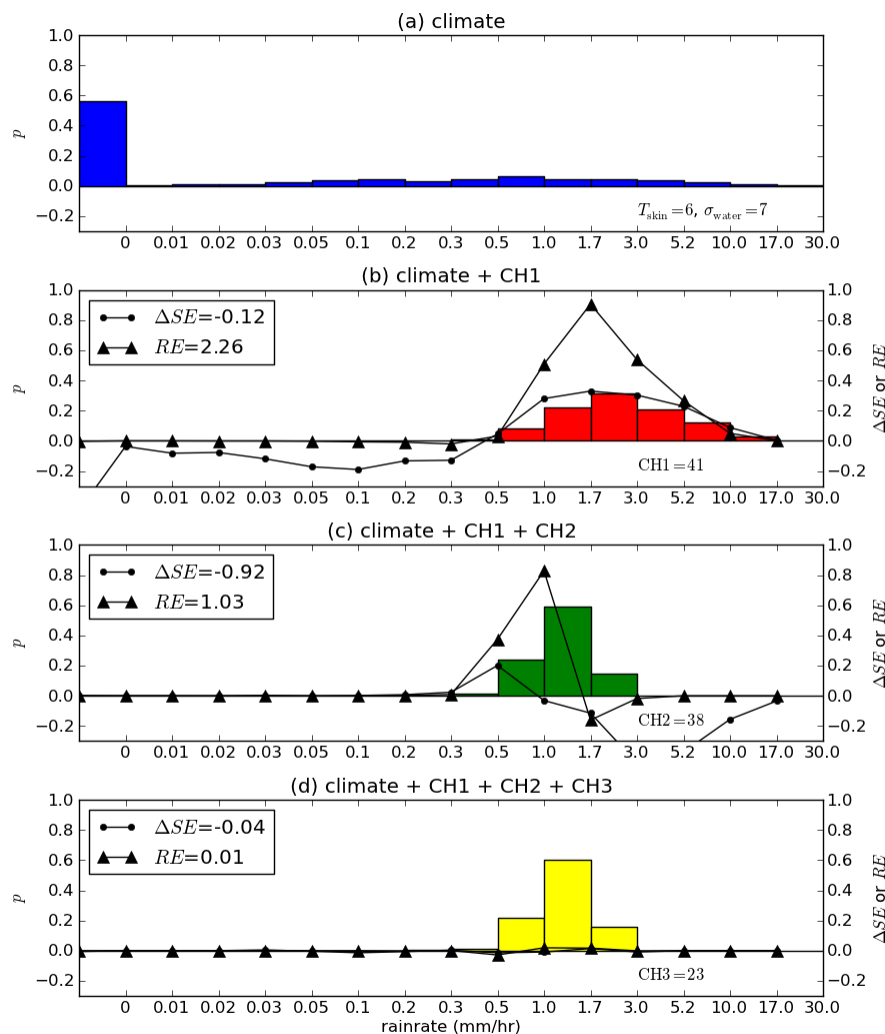


Figure 4-3: Probability distribution changes and information entropy changes with restrictions of CH1, CH2, and CH3. The land type is 0w. After scaling, $T_{\text{skin}} = 6$, $\sigma_{\text{water}} = 7$, $CH1 = 41$, $CH2 = 38$, $CH3 = 23$. Color blocks are probability within each bin, using the vertical axis to the left. The black triangle lines are relative entropy (RE). The black dotted lines are change of shannon entropy ΔSE . Both triangle and dotted lines follow the vertical coordinates to the right. Shown in each panels are: (a) only climate data, (b) climate data with CH1 restriction, (c) climate data with restrictions of CH1 and CH2, and (d) climate data with restrictions of CH1, CH2, and CH3.

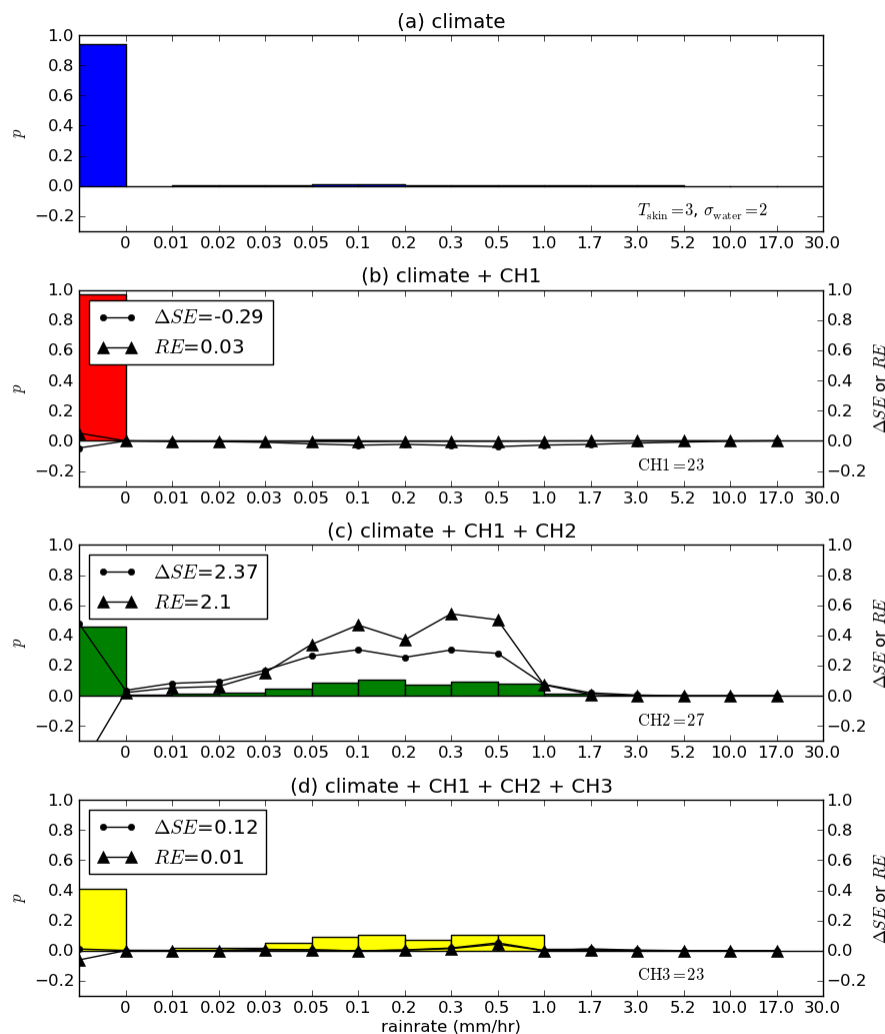


Figure 4-4: Probability distribution changes and information entropy changes with restrictions of CH1, CH2, and CH3. The land type is 0w. After scaling, $T_{skin} = 3$, $\sigma_{water} = 2$, $CH1 = 23$, $CH2 = 27$, $CH3 = 23$. Color blocks are probability within each bin, using the vertical axis to the left. The black triangle lines are relative entropy (RE). The black dotted lines are change of shannon entropy ΔSE . Both triangle and dotted lines follow the vertical coordinates to the right. Shown in each panels are: (a) only climate data, (b) climate data with CH1 restriction, (c) climate data with restrictions of CH1 and CH2, and (d) climate data with restrictions of CH1, CH2, and CH3.

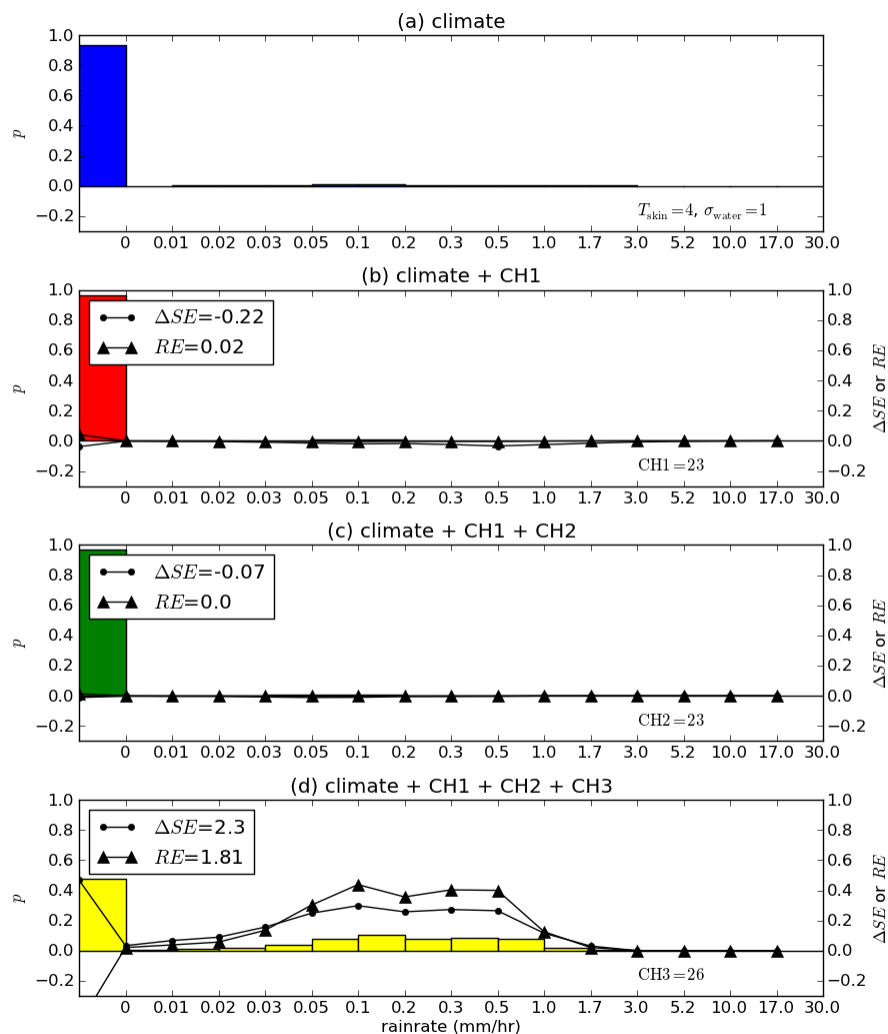


Figure 4-5: Probability distribution changes and information entropy changes with restrictions of CH1, CH2, and CH3. The land type is 0w. After scaling, $T_{\text{skin}} = 4$, $\sigma_{\text{water}} = 1$, $\text{CH1} = 23$, $\text{CH2} = 23$, $\text{CH3} = 26$. Color blocks are probability within each bin, using the vertical axis to the left. The black triangle lines are relative entropy (RE). The black dotted lines are change of shannon entropy ΔSE . Both triangle and dotted lines follow the vertical coordinates to the right. Shown in each panels are: (a) only climate data, (b) climate data with CH1 restriction, (c) climate data with restrictions of CH1 and CH2, and (d) climate data with restrictions of CH1, CH2, and CH3.

4.3 Necessity

In this section, both relative entropy and Shannon entropy are calculated under chosen environment variables and land types. When the prior retrieved results are altered to posterior ones by adding each pseudo-channel, both RE and ΔSE are evaluated to measure the information content of each pseudo-channel. Retrieved rain rate distributions are compared between posterior and prior to verify the quantification of information for each pseudo-channel. The goal of this section is to demonstrate the necessary condition of three successive pseudo-channels in terms of rain rate retrieval. In another words this section is to answer to what extent does each pseudo-channel contribute to the best to rain rate retrievals over different surface types.

4.3.1 CH1

CH1 is added to alter the retrieved rain rate from climate data that solely depends on the environmental variables (T_{skin} and σ_{water}) (Figure 4-6 4-7 and Table 4.1). For each surface type, the environmental variables that include the highest RE by adding CH1 is selected for the plots to show the CH1 information content. For example, Figure 4-6 with environmental variables of $T_{\text{skin}} = 6$ and $\sigma_{\text{water}} = 6$ has the largest Relative entropy ($RE = 5.79$ in Table 4.1) among other environmental variable values over the ocean.

In Figure 4-6, higher CH1 values corresponds with higher posterior² retrieved rain rates, which is depicted in (c) and (d), and higher CH1 values are responsible for a higher prior-posterior retrieved rain rate difference, which is depicted in (a) and (b). Reflected in the information content, generally lower CH1 samples have smaller

²posterior and prior are relative terms. In this section, retrievals before and after adding CH1 are considered prior and posterior respectively.

relative entropy values, higher CH1 samples have larger relative entropy. When CH1 in Figure 4-6 is small (ex. $15 \sim 25$), both prior and posterior rain rate probability distribution peak at zero or low rain rate bins (c) and (d). As CH1 increases (ex, $CH1 > 25$), more samples in the prior distributions are recognized by CH1 to have significantly larger rain rate. At the same time, more non-raining samples in the prior distributions are filtered by CH1. As a result, in Figure 4-6, peak of the rain rate distribution is shifted to higher rain rate bins as CH1 increases.

When CH1 is small (ex. $CH1 < 25$), negative ΔSE in Figure 4-6(f) depicts the dispersion reduction in the posterior retrieved rain rate distribution. Low CH1 values itself in Figure 4-6 (c) and (d) correspond with posterior low rain rates. It can be inferred that prior rain rate distribution before adding CH1 should peak at low or non-rain rate bins, so that the mean of prior rain rate distribution, as retrieved rain rate, can be close to zero in value. This inference of prior rain rate distribution is to certain extent reflected by Figure 4-3(a), 4-4(a), 4-5(a), where majority of samples are located at zero rain rate bin, although the environmental variables are not the same. In the posterior rain rate distribution, reduction of dispersion through CH1 further reflect the samples low or non rain rate features. In this way, a small CH1 value is considered as confirmation of little rain rate.

As $CH1 > 25$, ΔSE is positive (Figure 4-6(f)), which indicates an increase in dispersion of posterior rain rate distributions compared with prior ones. At large CH1 values in Figure 4-6 (ex. $25 \sim 40$ in (f)) the possibility of non-rain or little rain rate is reduced, and the samples with moderate or large rain rates are left and appear diverse in rain rate probabilities despite the fact they share similar CH1 values.

It is also interesting to notice that as $CH1 > 27$ in Figure 4-6(f), ΔSE turns less positive as CH1 increase in value. As CH1 increases beyond $CH1 = 27$, more samples of high rain rates are left from the prior distribution due to their high CH1 value, and

more samples of moderate rain rates are filtered due to their low CH1 value, and the rain rate distribution is shifted towards the higher rain rate, as reflected in Figure 4-6(c) and (d). In another words, high rain rates samples are less diverse when they share similar CH1 value (ex, $CH1 > 40$), and samples with moderate and low rain rates are more diverse when they share similar CH1 value (ex, $25 < CH1 < 30$).

As a sum-up, to retrieve rain rate, CH1 serves to correct the climate-data based Bayesian algorithm more at higher rain rate bins. For lower rain rate samples, adding CH1 provides confirmation to the retrieval based on climate-data, simply because lower rain rate samples are highly likely to have low CH1 values. Besides, CH1 is better to exclusively determine the high rain rate samples than it does to do moderate or low rain rate samples. Lower or moderate rain rate samples sharing same CH1 have more diverse rain rate distribution than high rain rate ones do sharing same CH1.

Figure 4-7 is plotted to depict the information content associated with prior-posterior retrieved rain rate difference over the warm vegetable land. Similar trend of CH1 over warm vegetable land is found as it is in ocean surface.

For some other surfaces types such as 1w, 1c, 2w, and 4w, in Table 4.1, similar trends are found as 0w, that CH1 provides more information on higher rain rate bins. For some surface types, the numbers of chosen samples are so limited, not enough to present a trend, such as 2c, 3w, 3c, 4c, 5w, 5c, 6w, and 6c. Table 4.1 collects all the surface types with the largest relative entropy values in each surface, to more efficiently illustrate the necessary value of CH1 quantified in information content. In Table 4.1 for retrievals in surface types 2c, 3c, 5w, 5c, 6w, and 6c, CH1 plays a role as confirmation to the low rain rates, reflected by little *RE* values. In Table 4.1 for retrievals in surface types 1w, 1c, 2w, 3w, and 4w, CH1 appears to alter the posterior rain rate distributions in terms of shifting the signal, and increasing the dispersion

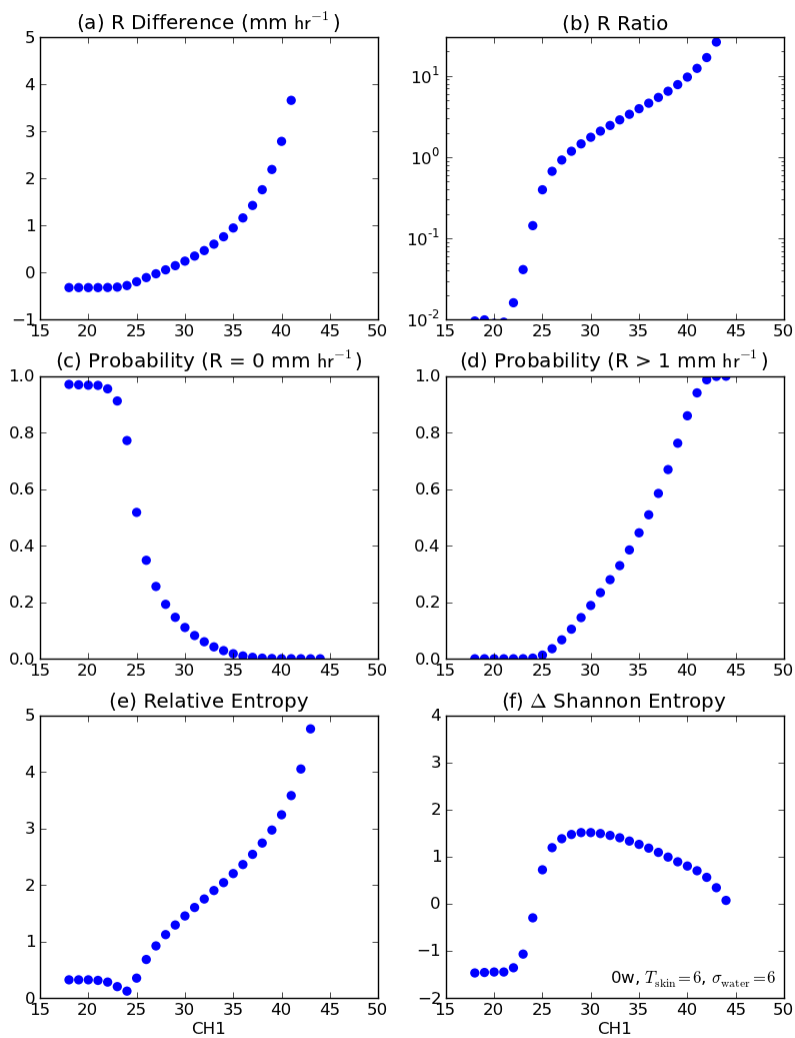


Figure 4-6: Rain rate information change by adding CH1 restriction. (a) average rain rate (R) difference, (b) average rain rate ratio, (c) probability of $R = 0$, (d) probability of $R > 1 \text{ mm hr}^{-1}$, (e) relative entropy after adding CH1, and (f) Shannon entropy difference after adding CH1. The land type is 0w. Environmental variables: $T_{\text{skin}} = 6$, $\sigma_{\text{water}} = 6$ after scaling.

from prior distributions. In Table 4.1 for retrievals in surface types 1w, 1c, 2w, 3w, and 4w, the retrieved rain rates after adding CH1 appear to be small or moderate in quantities. Reflected by ΔSE , adding CH1 in surface type 1w, 1c, 2w, 3w, and 4w in Table 4.1 increases the diversity of samples with low or moderate rain rate. It is worth to notice that Table 4.1 displays the case of adding CH1 with the highest relative entropy in each surface. Lower RE values of CH1 in different surface types, similar to the previous analysis on Figure 4-6, indicate CH1 as confirmations of lower rain rate feature.

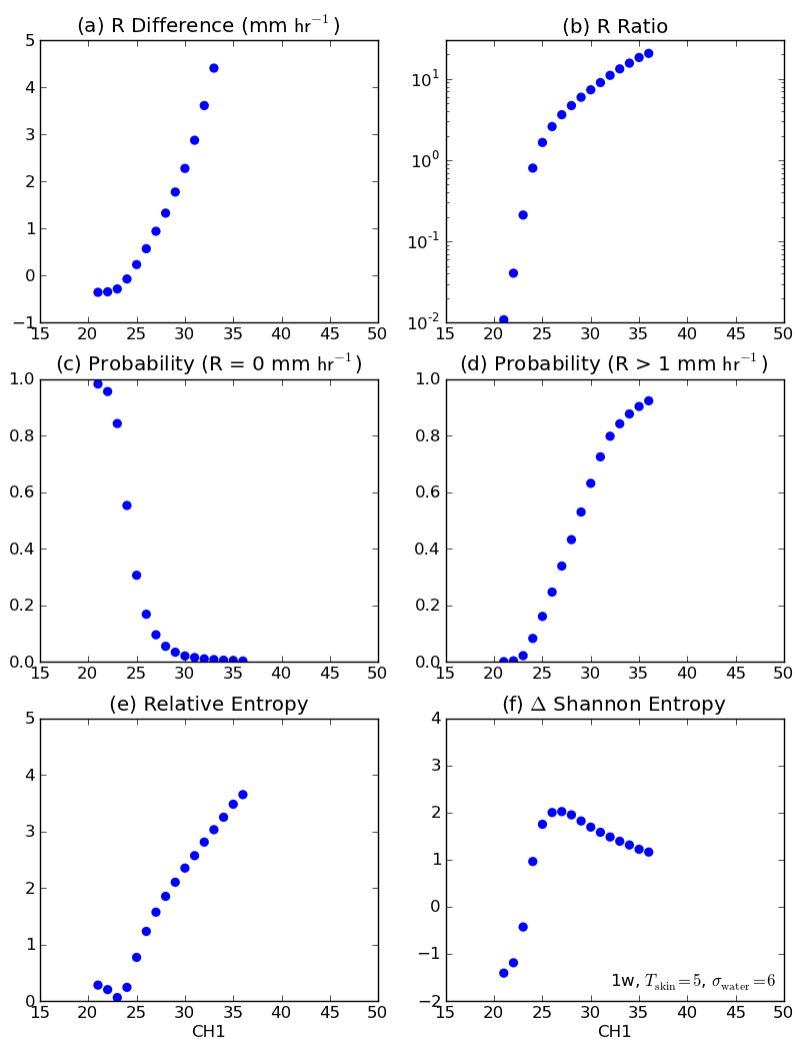


Figure 4-7: Same as above. The land type is 1w. Environmental variables: $T_{skin} = 5$, $\sigma_{water} = 6$ after scaling.

Surface	T_{skin}	σ_{water}	CH1	R Diff.	R Ratio	$P(R = 0 \text{ mm hr}^{-1})$	$P(R > 1 \text{ mm hr}^{-1})$	RE	ΔSE
0w	6	6	44	12.27	39.14	0.00	1.00	5.79	0.07
1w	5	6	36	7.04	20.60	0.00	0.92	3.65	1.16
1c	11	2	25	0.20	7.97	0.48	0.06	1.09	2.06
2w	6	6	32	2.82	9.92	0.01	0.69	2.61	1.61
2c	11	1	21	-0.01	0.04	0.99	0.00	0.02	-0.16
3w	6	3	26	0.49	27.60	0.29	0.13	2.78	3.04
3c	11	1	25	0.01	4.89	0.93	0.00	0.08	0.43
4w	5	6	27	0.55	2.41	0.14	0.25	1.22	1.91
4c	-	-	-	-	-	-	-	-	-
5w	1	1	24	0.02	2.22	0.89	0.00	0.05	0.43
5c	11	1	25	0.02	5.05	0.88	0.00	0.14	0.63
6w	3	2	22	-0.04	0.28	0.94	0.00	0.04	-0.43
6c	11	1	21	-0.01	0.56	0.97	0.00	0.01	-0.12

Table 4.1: Maximum retrieved rain rate changes in posterior probability distributions by adding CH1 under various surface types. The columns are denoted as (from left to right): surface categories, surface skin temperature, total precipitable water, CH1, rain rate difference (posterior - prior), rain rate ratio (posterior/prior), probability of posterior rain rate equal to zero mm/hr, probability of posterior rain rate greater than 1 mm/hr, relative entropy, and Shannon entropy difference. The threshold of sample numbers in this analysis is 1000 samples. All cases in 4c have less than the threshold, therefore, the 4c cases cannot be considered statistically representative.

4.3.2 CH2

CH2 is added to alter the retrieved rain rate from ‘climate+CH1 data’ that depends on both environmental variables and CH1 (Figure 4-8, 4-9 and Table 4.2). Alike previous section about CH1, for each surface type, the environmental variables that include the highest RE by adding CH2 is selected to show the CH2 information content. For example, Figure 4-8 with environmental variables of $T_{\text{skin}} = 6$ and $\sigma_{\text{water}} = 6$ has the largest Relative entropy ($RE = 1.22$ in Table 4.2) among other environmental variable values over the ocean. It is worth noticing that the scatter plots for CH2 are two dimensional, because both CH1 and CH2 are variables for information content even though environmental variables are settled.

In Figure 4-8, higher CH1 values correspond with higher retrieved rain rate distributions according to (c) and (d). The rain rate varies with CH2 quite weakly in Figure 4-8(c) and (d) compared with it does with CH1. When CH1 is large (ex. $30 < \text{CH1} < 40$ in Figure 4-8(d)), CH2 decreases as more samples have rain rates larger than 1mm hr^{-1} . When CH1 is small (ex. $\text{CH1} < 25$ in Figure 4-8(c)), CH2 increases as less samples have zero rain rates, which is opposite in trend from large CH1 mentioned previously.

In Figure 4-8(a) and (b), when CH1 is large (ex. $30 < \text{CH1} < 40$), CH2 alters the retrieved rain rate from prior distribution³. For example, at $\text{CH1} = 40$ and $\text{CH2} = 35$ in Figure 4-8(a) and (b), the posterior distribution estimates a lower rain rate than prior distribution does by adding CH2. At $\text{CH1} = 40$ and $\text{CH2} = 17$ in Figure 4-8(a) and (b), the posterior distribution estimates a higher rain rate than prior distribution does by adding CH2. Reflected in information content (Figure 4-8(e)), positive RE at

³To calculate retrieved rain rate, the mean is taken from the rain rate distribution. In this section, prior and posterior are relative terms indicating the distributions before and after adding CH2 respectively.

large CH1 (ex. $30 < \text{CH1} < 40$) shows signal shifts in rain rate distribution, where the upper positive anomaly ($\text{CH2} = 35$) indicates a shift to a lower rain rate, and bottom positive anomaly ($\text{CH2} = 17$) indicates a shift to a higher rain rate according to (c) and (d). In Figure 4-8(f), negative ΔSE at large CH1 (ex. $30 < \text{CH1} < 40$) shows less dispersion in distribution after adding CH2 compared with prior distribution.

When CH1 is small (ex, $\text{CH1} < 25$), CH2 changes the rain rate distribution. In Figure 4-8(e), when $\text{CH1} = 20, \text{CH2} = 27$, a significant positive RE indicates a signal shift of rain rate from the prior distribution. The change of distribution of $\text{CH1} = 20, \text{CH2} = 27$ can be reflected by increased rain rate ratio at same spot in Figure 4-8(b). ΔSE in Figure 4-8(f) shows positive anomaly at $\text{CH1} = 20, \text{CH2} = 27$, which indicates a larger dispersion in the posterior distribution than the prior one. Negative ΔSE at $\text{CH1} = 25, \text{CH2} = 20$ in Figure 4-8(f) indicates the posterior distribution, the rain rate dispersion is less spread out, where higher probability of non-rain samples are left in the posterior distribution after adding CH2. In Figure 4-8(f), the abrupt ΔSE anomaly at $20 < \text{CH1} < 25$, which is reflected correspondingly in (b) and (e), suggests an independent raining mechanism that involves envil clouds and produce little rain fall.

In short, Figure 4-8 shows the rain rate distribution change by adding CH2 over the ocean. CH2 over the ocean is observed to change the signal of rain rate PDF at higher retrieved rain rate samples. For lower rain rate samples, CH2 seems to be able to reflect different low rain rate precipitation types by ice.

Figure 4-9 shows the precipitation change by adding CH2 over warm vegetated land (1w) for a set of chosen environmental variables. The environmental variables $T_{\text{skin}} = 5$ and $\sigma_{\text{water}} = 6$ were chosen for the plot because the case under such environment variables contains the largest RE value for CH2 to have the biggest signal change on posterior rain rate probability distribution. In Figure 4-9(c), for low

rain rate samples ($CH1 < 25$), little variation of rain rate is shown along CH2 axis. In another words, CH2 reflect little on low rain rate variation. In Figure 4-9(d), for high rain rate samples ($CH1 > 25$), CH2 shows to reflect rain rate probability density variation for a chosen CH1. For example, when $CH1 = 30$ and $CH2 = 20$, more samples have rain rate over 1mm hr^{-1} than they do when $CH1 = 30$ and $CH2 = 27$ in Figure 4-9(d). Figure 4-9(d) shows that CH2 is responsible for more variation of moderate and high rain rates over warm vegetated land than it is for ocean.

Adding CH2 is shown to have larger RE at areas in Figure 4-9(e) when $CH1 > 25$ where lower than prior rain rate is evaluate due to higher CH2 value and higher than prior rain rate is evaluated due to smaller CH2 for the same CH1 values. In Figure 4-9(f), rain rate distribution has significant less dispersion to retrieve high rain rate.

Besides, data of other land types with largest RE in each case are listed in Table 4.2, which shows that CH2 gives the signal shift more in warm surfaces (0w, 1w, 2w, 3w, 4w), reflected by higher RE than cold surfaces (1c, 2c, 3c) and Tibetan/Himalayan range (5w, 5c, 6w, 6c). On average, the maximum RE by adding CH2 appears to be half or less than half as much as the maximum RE by adding CH1 (Table 4.1).

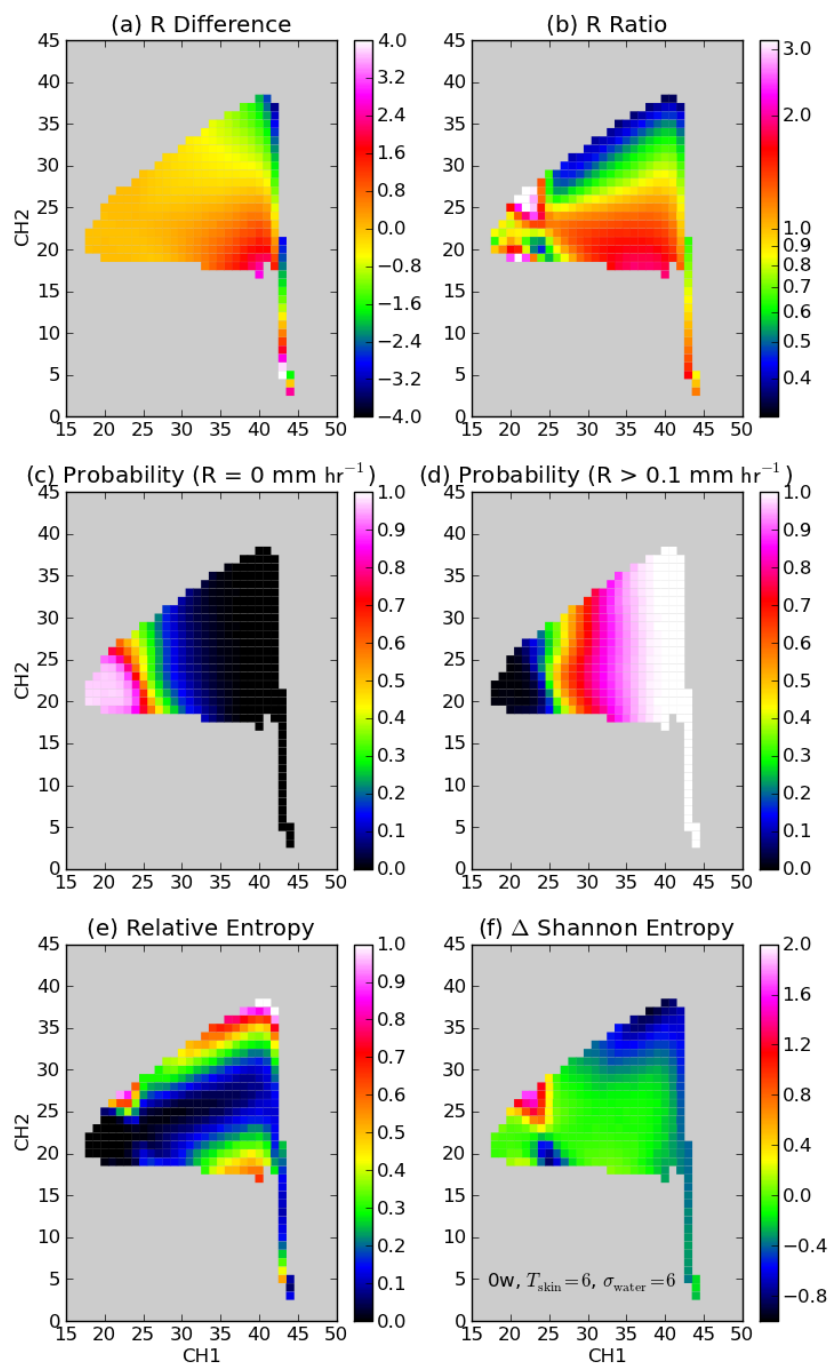


Figure 4-8: Rain rate information change by adding CH2 restriction. (a) average rain rate (R) difference, (b) average rain rate ratio, (c) probability of $R = 0$, (d) probability of $R > 1 \text{ mm hr}^{-1}$, (e) relative entropy after adding CH2, and (f) Shannon entropy difference from adding CH2. The default is $0w$. For information field

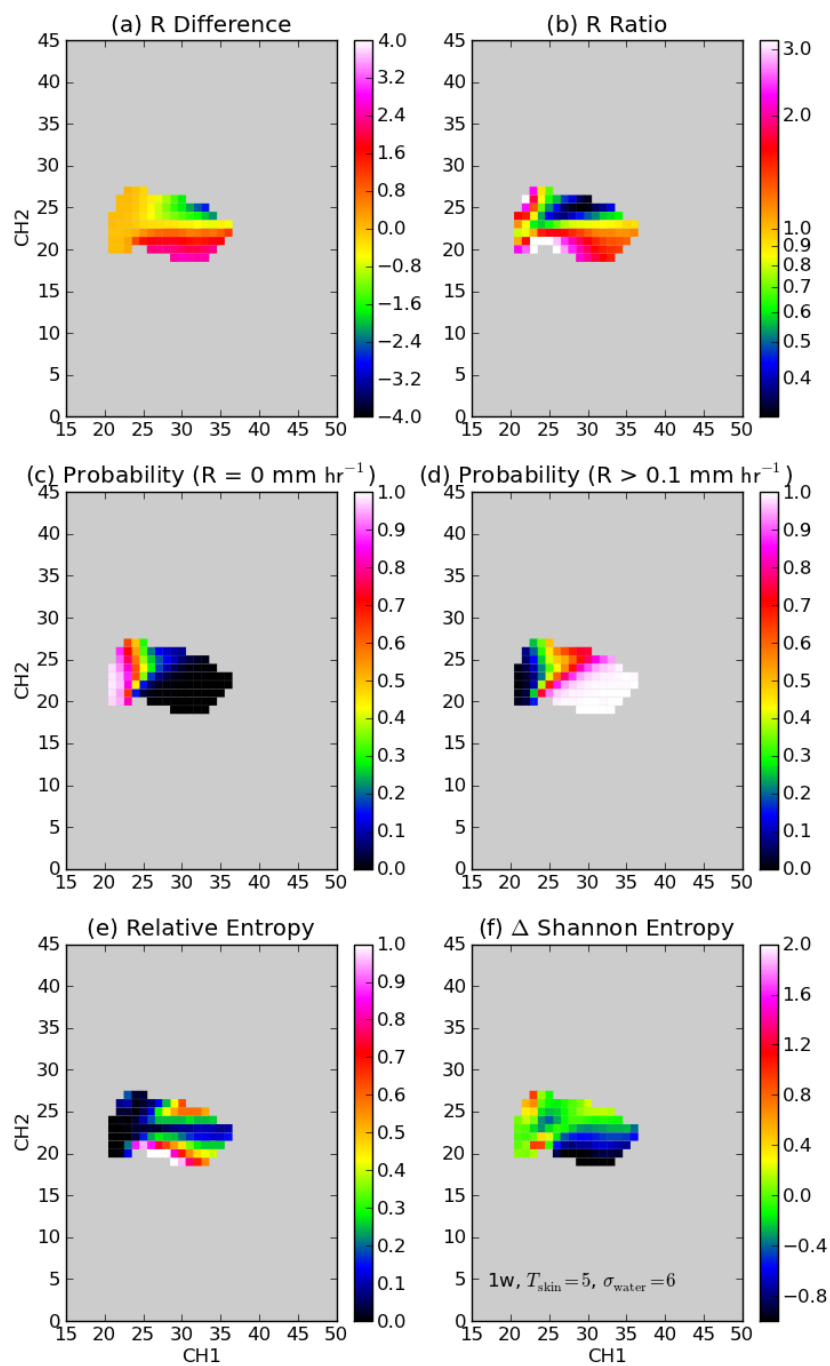


Figure 4-9: Same as above. The land type is 1w. Environmental variables: $T_{\text{skin}} = 5$, $\sigma_{\text{water}} = 6$.

Surface	T_{skin}	σ_{water}	CH1	CH2	R Diff.	R Ratio	$P(R = 0 \text{ mm hr}^{-1})$	$P(R > 0.1 \text{ mm hr}^{-1})$	RE	ΔSE
0w	6	6	42	37	-3.36	0.38	0.00	1.00	1.22	-0.70
1w	5	6	26	20	2.30	3.48	0.01	0.99	1.32	-0.86
1c	11	2	23	21	0.05	4.65	0.81	0.12	0.17	0.79
2w	6	6	23	25	0.19	7.07	0.55	0.35	0.78	1.71
2c	11	1	24	23	-0.01	0.36	0.98	0.01	0.02	-0.19
3w	3	2	25	25	0.29	3.66	0.33	0.51	0.81	1.74
3c	11	1	25	22	0.01	1.67	0.90	0.06	0.01	0.19
4w	5	5	22	25	0.06	8.85	0.77	0.15	0.42	1.18
4c	-	-	-	-	-	-	-	-	-	-
5w	2	1	24	24	0.03	2.21	0.81	0.12	0.06	0.51
5c	11	1	24	21	0.00	1.53	0.95	0.03	0.01	0.06
6w	5	2	23	23	-0.01	0.77	0.90	0.06	0.01	-0.05
6c	10	1	23	21	0.00	1.06	0.96	0.03	0.01	0.07

Table 4.2: Maximum retrieved rain rate changes in posterior probability distributions by adding CH2 under various surface types. The columns are denoted as (from left to right): surface categories, surface skin temperature, total precipitable water, CH1, CH2, rain rate difference (posterior - prior), rain rate ratio (posterior/prior), probability of posterior rain rate equal to zero mm/hr, probability of posterior rain rate greater than 0.1 mm/hr, relative entropy, and Shannon entropy difference. The threshold of sample numbers in this analysis is 1000 samples. All cases in 4c have less than the threshold, therefore, the 4c cases cannot be considered statistically representative.

4.3.3 CH3

Figure 4-10 (over the ocean), Figure 4-11 (over the warm vegetated land), and Table 4.3 (maximum RE over all land types) are shown to evaluate the information CH3 is added towards the rain rate retrievals. Figure 4-10 (over the ocean) and Figure 4-11 (over the warm vegetated land) are chosen because they both contain the largest RE values in each case, indicating the biggest signal changes from prior rain rate distribution to posterior one due to CH3. The prior rain rate probability distribution in this section refers to the rain rate distribution retrieved by environment variables (T_{skin} and σ_{water}), CH1, and CH2. The posterior rain rate probability distribution in this section refers to the rain rate distribution retrieved by environment variables (T_{skin} and σ_{water}), CH1, CH2, and CH3.

Over the ocean in Figure 4-10, large RE values in (e) (for example, CH3 = 26 and CH2 = 22) correspond with large rain ratio change in (b), where the rain rates are low or moderately low, according to (c) and (d). The ΔSE reflects an increase in dispersion in Figure 4-10(f) on the posterior distribution at places where RE is large in (e).

Over the land in Figure 4-11, large RE values in (e) (for example, CH3 = 26 and CH2 = 23) correspond with low rain rate signal shifted further towards lower end compared with prior distribution, which is reflected in small rain rate difference in (a) and small rain rate ratio (b) and high possibility of non-rain samples (c). The negative ΔSE in Figure 4-11(f) shows a shrink in dispersion on rain rate distribution, for example at CH3 = 26 and CH2 = 23. Both RE and ΔSE around CH3 = 26 and CH2 = 23 in Figure 4-11(e) and (f) indicates a confirmation of low rain rate samples.

In Table 4.3, the maximum RE values over all surface types are smaller than 1.0, not significant on altering the rain rate distribution signal shift.

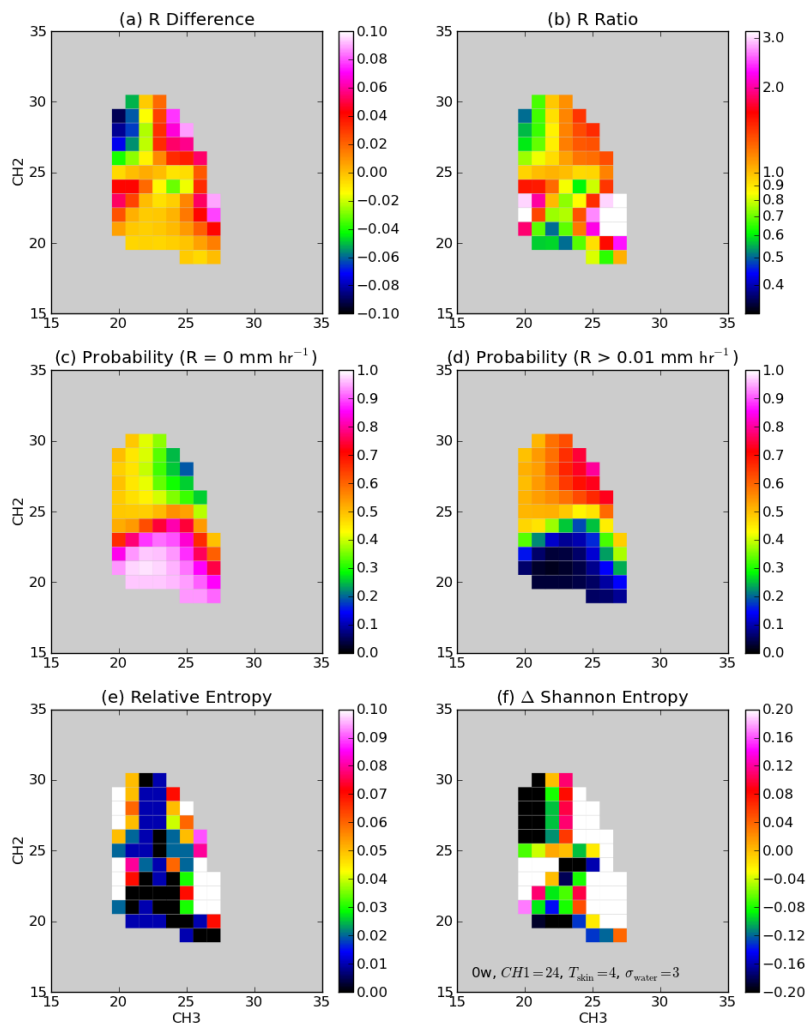


Figure 4-10: Rain rate information change by adding CH3 restriction. (a) average rain rate (R) difference, (b) average rain rate ratio, (c) probability of $R = 0$, (d) probability of $R > 1 \text{ mm hr}^{-1}$, (e) relative entropy after adding CH3, and (f) Shannon entropy difference after adding CH3. The land type is $0w$. $CH1 = 24$, Environmental variables: $T_{\text{skin}} = 4$, $\sigma_{\text{water}} = 3$ after scaling.

In short, CH3 doesn't appear to influence as significantly to rain rate retrievals as CH1 or CH2. The contribution of CH3 to rain rate retrieval is shown in this section to provide confirmation to the samples with low/zero rain rate.

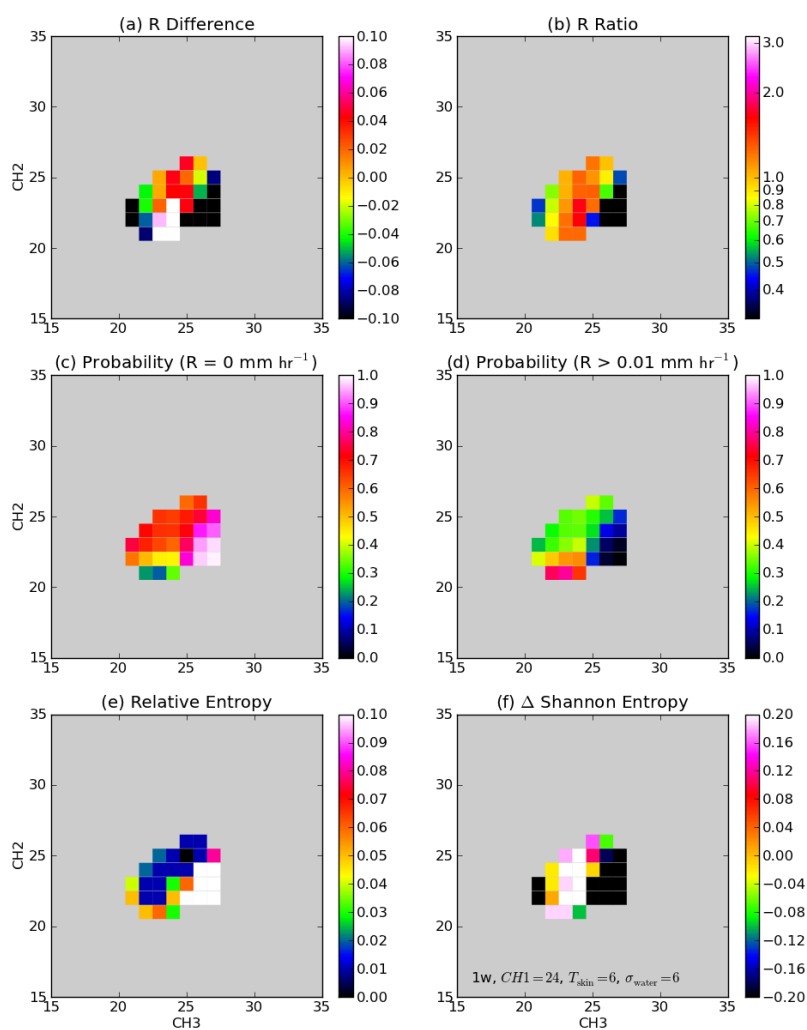


Figure 4-11: Same as above. The land type is 1w. $CH1 = 24$, Environmental variables: $T_{\text{skin}} = 6$, $\sigma_{\text{water}} = 6$ after scaling.

Surface	T_{skin}	σ_{water}	CH1	CH2	CH3	R Diff.	R Ratio	$P(R = 0 \text{ mm hr}^{-1})$	$P(R > 0.01 \text{ mm hr}^{-1})$	RE	ΔSE
0w	4	3	24	22	27	0.08	9.31	0.61	0.38	0.85	1.80
1w	6	6	24	22	27	-0.41	0.02	0.99	0.01	0.90	-2.59
1c	11	1	25	22	26	-0.05	0.09	0.98	0.02	0.15	-0.86
2w	6	6	25	22	24	0.81	4.25	0.30	0.69	0.53	1.10
2c	11	1	24	22	22	-0.00	0.54	0.98	0.02	0.01	-0.13
3w	4	2	23	24	25	0.07	11.04	0.78	0.22	0.41	1.19
3c	11	1	24	22	20	-0.00	0.70	0.99	0.01	0.02	-0.15
4w	5	5	23	22	25	0.07	3.39	0.84	0.15	0.09	0.60
4c	-	-	-	-	-	-	-	-	-	-	-
5w	1	1	23	23	21	-0.01	0.17	0.98	0.02	0.04	-0.34
5c	11	1	23	23	25	0.00	2.55	0.98	0.02	0.01	0.07
6w	2	2	22	23	21	0.01	1.58	0.94	0.06	0.01	0.03
6c	11	1	22	21	22	-0.00	0.69	0.97	0.03	0.01	-0.09

Table 4.3: Maximum retrieved rain rate changes in posterior probability distributions by adding CH3 under various surface

types. The columns are denoted as (from left to right): surface categories, surface skin temperature, total precipitable water, CH1, CH2, CH3, rain rate difference (posterior - prior), rain rate ratio (posterior/prior), probability of posterior rain rate equal to zero mm/hr, probability of posterior rain rate greater than 0.01 mm/hr, relative entropy, and Shannon entropy difference. The threshold of sample numbers in this analysis is 1000 samples. All cases in 4c have less than the threshold, therefore, the 4c cases cannot be considered statistically representative.

4.4 Sufficiency

In this section, the sufficiency of three successive pseudo-channels is evaluated by using bivariate histograms to compare the prior and posterior rain rate distributions when each pseudo-channel is successively added to the algorithm. Representative bivariate histograms are displayed in Figure 4-12 (over the ocean), Figure 4-13 (over the vegetated land), Figure 4-14 (over the land/water mix, coast), and Figure 4-15 (over all surface types). The goal of this section is to show whether three successive pseudo-channels are sufficient to retrieve the rain rate, is the fourth pseudo-channel necessary in terms of improving the precision of retrieved rain rates.

Over the ocean in Figure 4-12(a), from climatology to climatology and CH1, the samples are completely redistributed in the posterior bins. In Figure 4-12(b), from climatology + CH1 to climatology + Channel 1 and 2, adding CH2 doesn't change the rain rate distribution much when retrieved rain rate is above 0.2mm hr^{-1} , but CH2 changes the rain rate distribution significantly at among low rain rate samples. In Figure 4-12(c), the majority samples $O(10^8)$ are not significantly redistributed by adding CH3, which appears to be $y = x$ linear relationship in the diagram. There are some samples in the lower rain rate bins that are redistributed by CH3 in Figure 4-12(c), with around $O(10^3)$ or $O(10^4)$ samples.

Over the warm vegetated land in Figure 4-13(a), from climatology to climatology and CH1, the samples are largely redistributed in the posterior bins. In Figure 4-13(b), CH2 alters the distribution to an even spread almost along all the bins. In Figure 4-13(c), adding CH3 doesn't appear to change much on the higher end of the bins (ex. rain rate above 1.0mm hr^{-1}). At lower rain rate bins, majority ($O(10^8)$) of samples are not altered by adding CH3 in Figure 4-13(c), and some minor samples $O(10^3)$ are redistributed from moderate rain rate bins like 0.3mm hr^{-1} in prior to low

rain rate bins like 0.01mm hr^{-1} in posterior.

Over the warm land/water mix (coast) in Figure 4-14(a), like previous two cases, CH1 alters the distribution greatly. In Figure 4-14(b) and (c) CH2 and CH3 don't appear to alter the distribution much, as majority ($O(10^5)$) are on the $y = x$ line.

The bivariate for all surfaces classes are plotted in Figure 4-15. It is shown that in Figure 4-15(a), CH1 alters the distribution greatly from climatology to climatology and CH1. In Figure 4-15(b) and (c), CH2 and CH3 appear to alter little the majority ($O(10^8)$) of the samples. Samples of $O(10^3)$ are redistributed by CH3 among lower and moderate rain rate bins.

As a sum-up, in most of the cases examined so far over ocean and different land types, it appears that the majority of information affecting the posterior probability distribution of rain rate is found in the first two pseudo-channels. Dropping the third channel from the retrieval usually has only a minor effect on the retrieved probability distributions. But there are exceptions, especially for less common combinations of the first two channels.

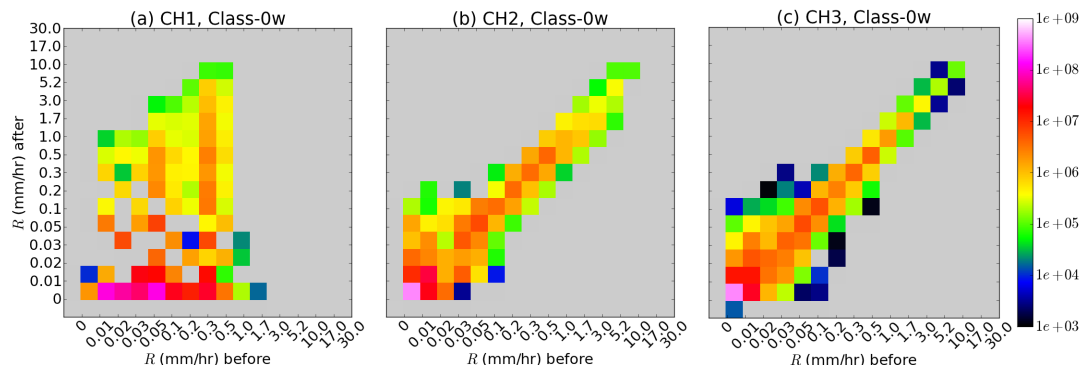


Figure 4-12: Bivariate histograms comparing distributions of rain rates prior to (horizontal axis) and following (vertical axis) the successive addition of channels, starting with Channel 1 relative to climatology (left), Channel 1+2 relative to Channel 1 only (center), Channels 1-3 relative to 1+2 (right). The surface type here is ocean (0w).

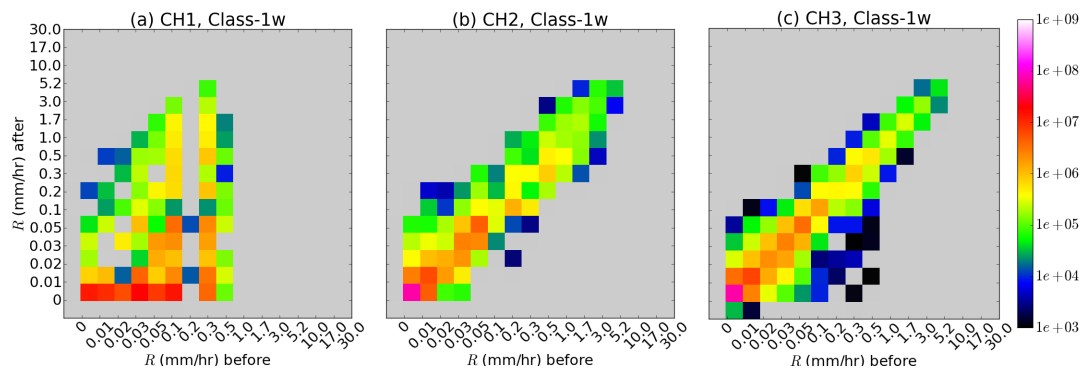


Figure 4-13: Same as above. The surface type here is warm vegetated land (1w).

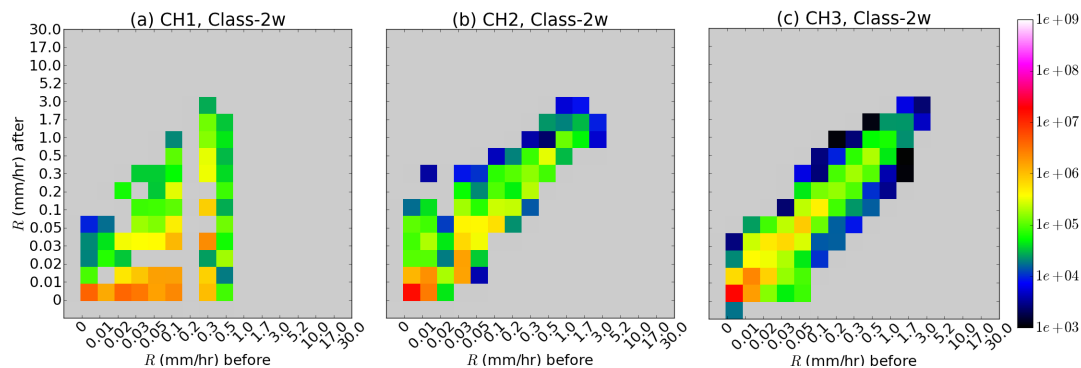


Figure 4-14: Same as above. The surface type here is warm land/water mix, coast (2w).

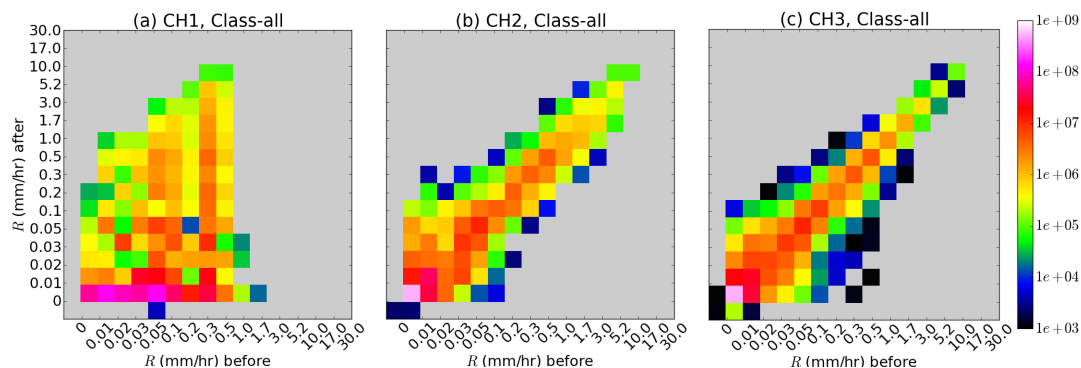


Figure 4-15: Same as above. It includes all surface types (0w, 1w, 1c, 2w, 2c, 3w, 3c, 4w, 4c, 5w, 5c, 6w, 6c), where surface 4c has zero selected samples for the statistics that are statistically representative.

Chapter 5

Conclusions

The UW algorithm was developed to retrieve rain rate from TMI, using reduced-dimensional Bayesian algorithm. Three pseudo-channels are generated mathematically using principle component analysis, presumably taking three most important roles to retrieve rain rate.

In this project, the information that three pseudo-channels provide are analyzed both qualitatively and quantitatively. Firstly, the physical meaning of the three pseudo-channels is demonstrated by using the Gram-Schmidt Process. The initial results suggest that over the ocean:

- CH1 is related to column rain water;
- CH2 is related to ice scattering aloft: negative CH2 is related to the ice in a convective storm, and positive CH2 is related to the ice in anvil clouds;
- CH3 responds to edges and gradients.

As part of the UW algorithm, rain rate probability distributions are calculated for chosen environmental variables and successive pseudo-channels. With this advantage, each of the three successive pseudo-channels are evaluated for the information contribution to the UW algorithm by keeping one pseudo-channels, two, or three and comparing the probability distributions between each other.

From Climatology to Climatology + CH1, adding CH1 provides the most dominant information to the rain rate distributions among all three pseudo-channels. CH1 itself increases as the posterior rain rate increases. CH1 provides more signal shift to the posterior rain rate distribution at larger CH1 values. The signal shift of the posterior rain rate distribution can be reflected by a increase or decrease on retrieved rain rate from posterior distribution in Bayesian algorithm, which is calculated as the average of the probability distribution. CH1 provides an increase in dispersion of posterior probability distribution at small CH1 values and a decrease in dispersion of posterior probability distribution at large CH1 values.

From Climatology + CH1 to Climatology + CH1 +CH2, adding CH2 provides some information to the rain rate distributions. For low CH1 values (low retrieved rain rate from posterior distribution), CH2 would correspond little variation with retrieved rain rate. For large CH1 values (high retrieved rain rate from posterior distribution), larger CH2 would correspond with a smaller retrieved rain rate. Adding CH2 would cause signal shift of rain rate distributions over all ranges of rain rate. CH2 can both increase the retrieved rain rate from prior distribution when CH2 is towards the high end and decrease the retrieved rain rate from prior distribution when CH2 is towards the low end.

From Climatology + CH1 + CH2 to Climatology + three successive pseudo-channels, most of the time, CH3 provides little information to the rain rate distributions. However, for certain cases with rare combinations of CH1 and CH2, CH3 may appear to provide significant information content.

As for evaluation on various surface types, all three successive pseudo-channels provide largest information content¹ over ocean, warm vegetated land, warm land/water

¹Over each surface type, the maximum relative entropy is ranked to evaluate information content each pseudo-channel provides. For CH1, the threshold for RE is set to be 1.0. For CH2, the threshold for RE is

mix (coast) and warm desert. Only CH1 and CH2 but CH3 provide significant information content over warm rain forest. Only CH1 but CH2 or CH3 provides significant information content over cold vegetated land. None of the three pseudo-channels appear to provide significant information content over cold land/water mix (coast), cold desert, Tibetan Plateau and similar, and Himalayan range and similar.

Bibliography

- Adler, R., C. Kidd, G. Petty, M. Morissey, and H. Goodman, 2001: Intercomparison of global precipitation products: The third Precipitation Intercomparison Project (PIP-3). *Bull. Amer. Meteor. Soc.*, **82** (7), 1377–1396.
- Aonashi, K., A. Shibata, and G. Liu, 1996: An over-ocean precipitation retrieval using SSM/I multichannel brightness temperatures. *J. Meteor. Soc. Japan*, **74**, 617–637.
- Barrett, E., C. Kidd, and D. Kniveton, 10-14 Jul. 1995: The first WetNet Precipitation Intercomparison Project (PIP-1): reflections on the results. *Geoscience and Remote Sensing Symposium, 1995. IGARSS '95. 'Quantitative Remote Sensing for Science and Applications', International*, **1**, 649–651 vol.1.
- Basist, A., N. Grody, T. Peterson, and C. Williams, 1998: Using the Special Sensor Microwave/Imager to monitor land surface temperatures, wetness and snow cover. *J. Appl. Meteor.*, **37** (9), 888–911.
- Bauer, P., P. Amayenc, C. Kummerow, and E. Smith, 2001: Over-ocean rainfall retrieval from multisensor data of the Tropical Rainfall Measuring Mission. Part II: Algorithm implementation. *J. Atmos. Ocean Technol.*, **18** (11), 1838–1855.
- Bayes, T. and R. Price, 1763: An essay towards solving a problem in the doctrine of chances. by the late rev. mr. bayes, f. r. s. communicated by mr. price, in a letter to john canton, a. m. f. r. s. *Philosophical Transactions*, **53**, 370–418, doi:10.1098/rstl.1763.0053, URL <http://rstl.royalsocietypublishing.org/>

content/53/370.short, <http://rstl.royalsocietypublishing.org/content/53/370.full.pdf+html>.

Bennartz, R. and G. Petty, 2001: The sensitivity of microwave remote sensing observations of precipitation to ice particle size distributions. *J. Appl. Meteor.*, **40** (3), 345–364.

Chaloner, K. and I. Verdinelli, 1995: Bayesian experimental design: A review. *statistical science*. **10** (3), 273–304.

Chiu, J.-Y. and G. Petty, 2006: Bayesian retrieval of complete posterior PDFs of oceanic rain rate from microwave observations. *J. Appl. Meteor. Climat.*, **45** (8), 1073–1095.

Chiu, L. S., G. R. North, D. A. Short, and A. McConnell, 1990: Rain estimation from satellites: Effects of finite field of view. *J. Geophys. Res.*, **95** (2177–2185).

Conner, M. and G. Petty, 1998: Validation and intercomparison of SSM/I rain-rate retrieval methods over the continental United States. *J. Appl. Meteor.*, **37** (7), 679–700.

Cooper, S. J., T. S. L’Ecuyer, P. Gabriel, A. J. Baran, and G. L. Stephens, 2005: Objective assessment of the information content of visible and infrared radiance measurements for cloud microphysical property retrievals over the global oceans. part ii: Ice clouds. *J. Appl. Meteor. Climat.*, **45**, 42–62.

Dee, D. P., et al., 2011: The ERA-Interim reanalysis: configuration and performance of the data assimilation system. *Q.J.R. Meteorol. Soc.*, **137**, 553–597.

Di Michele, S., A. Tassa, A. Mugnai, F. Marzano, P. Bauer, and J. Baptista, 2005: Bayesian algorithm for microwave-based precipitation retrieval: Description and

- application to TMI measurements over ocean. *IEEE Trans. Geosci. Remote Sensing*, **43** (4), 778–791.
- Ebert, E., M. Manton, P. Arkin, R. Allam, G. Holpin, and A. Gruber, 1996: Results from the GPCP algorithm intercomparison programme. *Bull. Amer. Meteor. Soc.*, **77**, 2875–2887.
- Evans, K., J. Turk, J. Wong, and T. Stephens, 1995: A Bayesian approach to microwave precipitation profile retrieval. *J. Appl. Meteor.*, **34**, 260–279.
- Ferraro, R., W. F.Z., G. N.C., and B. A., 1996: An eight-year (1987-1994) time series of rainfall, clouds, water vapor, snow cover, and sea ice derived from ssm/i measurements. *Bull. Amer. Meteor. Soc.*, **77** (5), 891–905.
- Ferraro, R. and Q. Li, 2002: Detailed analysis of the error associated with the rainfall retrieved by the NOAA/NESDIS Special Sensor Microwave/Imager algorithm 2. Rainfall over land. *J. Geophys. Res.-Atmos.*, **107** (D23).
- Ferraro, R., E. Smith, W. Berg, and G. Huffman, 1998: A screening methodology for passive microwave precipitation retrieval algorithms. *J. Atmos. Sci.*, **55** (9), 1583–1600.
- Fisher, R. A., 1956: *Statistical Methods and Scientific Inference*. Oliver and Boyd, London.
- Frigg, R. and C. Werndl, 2011: *Entropy—A Guide for the Perplexed*. Oxford University Press.
- Gloersen, P. and F. Barath, 1977: A scanning multichannel microwave radiometer for Nimbus-G and Seasat-A. *IEEE J. of Ocean. Eng.*, **OE-2**, 172–178.

- Greco, M. and E. Anagnostou, 2002: Use of passive microwave observations in a radar rainfall-profiling algorithm. *J. Appl. Meteor.*, **41** (7), 702–715.
- Greco, M. and W. Olson, 2006: Bayesian estimation of precipitation from satellite passive microwave observations using combined radar-radiometer retrievals. *J. Appl. Meteor. Climat.*, **45** (3), 416–433.
- Greco, M., W. Olson, and E. Anagnostou, 2004: Retrieval of precipitation profiles from multiresolution, multifrequency active and passive microwave observations. *J. Appl. Meteor.*, **43** (4), 562–575.
- Grody, N. C., 1991: Classification of snow cover and precipitation using the Special Sensor Microwave Imager. *J. Geophys. Res.*, **96** (4), 7423–7435.
- Ha, E. and G. R. North, 1995: Model studies of the beam-filling error for rain-rate retrieval with microwave radiometers. *J. Atmos. Ocean Technol.*, **12** (268–281).
- Haddad, Z., E. Smith, C. Kummerow, T. Iguchi, M. Farrar, S. Durden, M. Alves, and W. Olson, 1997: The TRMM ‘day-1’ radar/radiometer combined rain-profiling algorithm. *J. Meteor. Soc. Japan*, **75** (4), 799–809.
- Hollinger, J., 1989: DMSF Special Sensor Microwave/Imager Calibration/Validation, Final Report Vol. I. Tech. rep.
- Huffman, G. J. and Coauthors, 1997: The global precipitation climatology project (gpcp) combined precipitation dataset. *Bull. Amer. Meteor. Soc.*, **78** (5-20).
- Jeffreys, H., 1945: An invariant form for the prior probability in estimation problems. *Proceedings of the Royal Society of London. Series A, Mathematical and Physical Sciences*, **186** (1007), 453–461.

- Kida, S., S. Shige, T. Kubota, K. Aonashi, and K. Okamoto, 2009: Improvement of rain/no-rain classification methods for microwave radiometer observations over the ocean using a 37 Ghz emission signature. *J. Meteor. Soc. Japan*, **87** (Sp. Iss. SI), 165–181.
- Kidd, C., 1998: On rainfall retrieval using polarization-corrected temperatures. *Int. J. Remote Sens.*, **19** (5), 981–996.
- Kullback, S., 1997: *Information Theory and Statistics*. Dover Publications, INC.
- Kullbak, S. and R. A. Leibler, 1951: On information and sufficiency. *The Annals of Mathematical Statistics*, **22** (1), 79–86.
- Kummerow, C., 1993: On the accuracy of the eddington approximation for radiative-transfer in the microwave-frequencies. *J. Geophys. Res. Atmos.*, **98** (D2), 2757–2765.
- Kummerow, C., 1998: Beamfilling errors in passive microwave rainfall retrievals. *J. Appl. Meteor.*, **37** (4), 356–370.
- Kummerow, C., 2006: TRMM TMI Level 1C Development. URL http://mrain.atmos.colostate.edu/LEVEL1C/level1C_devtmi.html.
- Kummerow, C., W. Barnes, T. Kozu, J. Shiue, and J. Simpson, 1998: The Tropical Rainfall Measuring Mission (TRMM) sensor package. *J. Atmos. Ocean Technol.*, **15** (3), 809–817.
- Kummerow, C., W. Berg, J. Thomas-Stahle, and H. Masunaga, 2006: Quantifying global uncertainties in a simple microwave rainfall algorithm. *J. Atmos. Ocean Technol.*, **23** (1), 23–37.

- Kummerow, C. and Coauthors, 2001: The evolution of the goddard profiling algorithm (gprof) for rainfall estimation from passive microwave sensors. *J. Appl. Meteor.*, **40**, 1801–1820.
- Kummerow, C., S. Finn, J. Crook, D. Randel, and W. Berg, 2009: An observationally based a-priori database for bayesian rainfall retrievals. *J. Clim. Appl. Meteor.* (*submitted*).
- Kummerow, C. and L. Giglio, 1994a: A passive microwave technique for estimating rainfall and vertical structure information from space. Part II: Applications to SSM/I data. *J. Appl. Meteor.*, **33** (1), 19–34.
- Kummerow, C. and L. Giglio, 1994b: A passive microwave technique for estimating rainfall and vertical structure information from space. Part I: Algorithm description. *J. Appl. Meteorol.*, **33** (1), 3–18.
- Kummerow, C., H. Masunaga, and P. Bauer, 2007: A next-generation microwave rainfall retrieval algorithm for use by TRMM and GPM. *Measuring Precipitation from Space: EURAINSAT and the Future*, Levizzani, V and Bauer, P and Turk, FJ, Ed., Springer, Advances in Global Change Research, Vol. 28, 235+.
- Kummerow, C., W. Olson, and L. Giglio, 1996: A simplified scheme for obtaining precipitation and vertical hydrometeor profiles from passive microwave sensors. *IEEE Trans. Geosci. Remote Sensing*, **34** (5), 1213–1232.
- Kummerow, C. and P. Poyner, 2004: The effects of rainfall inhomogeneity on climate variability of rainfall estimated from passive microwave sensors. *J. Atmos. Ocean. Tech.*, **21** (4), 624–638.
- Kummerow, C., et al., 2000: The status of the Tropical Rainfall Measuring Mission (TRMM) after two years in orbit. *J. Appl. Meteor.*, **39** (12), 1965–1982.

- Kummerow, C., et al., 2001: The evolution of the Goddard profiling algorithm (GPROF) for rainfall estimation from passive microwave sensors. *J. Appl. Meteor.*, **40** (11), 1801–1820.
- Kummerow, C. D., S. Ringerud, J. Crook, D. Randel, and W. Berg, 2011: An observationally generated a priori database for microwave rainfall retrievals. *J. Atmos. Ocean Technol.*, **28** (2), 113–130.
- L’Ecuyer, T., P. Gabriel, K. Leesman, S. J. Cooper, and G. L. Stephens, 2005: Objective assessment of the information content of visible and infrared radiance measurements for cloud microphysical property retrievals over the global oceans. part i: Liquid clouds. *J. Appl. Meteor. Climat.*, **45**, 20–41.
- L’Ecuyer, T. and G. Stephens, 2002: An uncertainty model for Bayesian Monte Carlo retrieval algorithms: Application to the TRMM observing system. *Quart. J. Roy. Meteor. Soc.*, **128** (583), 1713–1737.
- Liu, G. and J. A. Curry, 1992: Retrieval of precipitation from satellite microwave measurement using both emission and scattering. *J. Geophys. Res.*, **97** (9), 9959–9974.
- Marshall, J. and W. Palmer, 1948: The distribution of raindrops with size. *J. Meteor.*, **5**, 165–166.
- Marzano, F., A. Mugnai, G. Panegrossi, N. Pierdicca, E. Smith, and J. Turk, 1999: Bayesian estimation of precipitating cloud parameters from combined measurements of spaceborne microwave radiometer and radar. *IEEE Trans. Geosci. Remote Sensing*, **37** (1, Part 2), 596–613.
- Masunaga, H. and C. Kummerow, 2005: Combined radar and radiometer analysis of

- precipitation profiles for a parametric retrieval algorithm. *J. Atmos. Ocean Technol.*, **22** (7), 909–929.
- McCollum, J. and R. Ferraro, 2005: Microwave rainfall estimation over coasts. *J. Atmos. Ocean. Tech.*, **22** (5), 497–512.
- Olson, W., C. Kummerow, G. Heymsfield, and L. Giglio, 1996: A method for combined passive–active microwave retrievals of cloud and precipitation profiles. *J. Appl. Meteor.*, **35**, 1763–1789.
- Olson, W., et al., 2006: Precipitation and latent heating distributions from satellite passive microwave radiometry. Part I: Improved method and uncertainties. *J. Appl. Meteor. Climat.*, **45** (5), 702–720.
- Panegrossi, G., et al., 1998: Use of cloud model microphysics for passive microwave-based precipitation retrieval: Significance of consistency between model and measurement manifolds. *J. Atmos. Sci.*, **55**, 1644–1673.
- Petrenko, B., 2001: Retrieval of parameters of a horizontal hydrometeor distribution within the field of view of a satellite microwave radiometer. *IEEE T. Geosci. Remote*, **39** (9), 1871–1878.
- Petty, G., 1994a: Physical retrievals of over-ocean rain rate from multichannel microwave imagery. Part I: Theoretical characteristics of normalized polarization and scattering indices. *Meteorol. Atmos. Phys.*, **54** (1–4), 79–100.
- Petty, G., 1994b: Physical retrievals of over-ocean rain rate from multichannel microwave imagery. Part II: Algorithm implementation. *Meteorol. Atmos. Phys.*, **54** (1–4), 101–121.
- Petty, G., 2001: Physical and microwave radiative properties of precipitating clouds.

- Part I: Principal component analysis of observed multichannel microwave radiances in tropical stratiform rainfall. *J. Appl. Meteorol.*, **40**, 2105–2114.
- Petty, G., 2006: *A First Course in Atmospheric Radiation (2nd Ed.)*. Sundog Publishing, Madison, WI.
- Petty, G., 2012: Dimensional reduction in bayesian retrievals. *J. Atmos. Ocean. Tech.*
- Petty, G. and K. Li, 2013a: Improved passive microwave precipitation retrievals over land and ocean. 1. Algorithm description. *J. Atmos. Ocean. Technol.*, (conditionally accepted).
- Petty, G. and K. Li, 2013b: Improved passive microwave precipitation retrievals over land and ocean. 2. Validation and intercomparison. *J. Atmos. Ocean Technol.*, (conditionally accepted).
- Petty, G. W., 2013: Dimensionality reduction in Bayesian estimation algorithms. *Atmospheric Measurement Techniques Discussions*, **6 (2)**, 2327–2352, doi:10.5194/amtd-6-2327-2013, URL <http://www.atmos-meas-tech-discuss.net/6/2327/2013/>.
- Prabhakara, C., G. Dalu, G. Liberti, J. Nucciarone, and R. Suhasini, 1992: Rainfall estimation over oceans from SMMR and SSM/I microwave data. *J. Appl. Meteorol.*, **31 (6)**, 532–552.
- Prigent, C., J. Pardo, M. Mishchenko, and W. Rossow, 2001: Microwave polarized signatures generated within cloud systems: Special Sensor Microwave Imager (SSM/I) observations interpreted with radiative transfer simulations. *J. Geophys. Res. Atmos.*, **106 (D22)**, 28 243–29 258.
- Schols, J., J. Weinman, G. Alexander, R. Stewart, L. Angus, and A. Lee, 1999:

- Microwave properties of frozen precipitation around a north atlantic cyclone. *J. Appl. Meteor.*, **38**, 29–43.
- Seo, E.-K., B.-J. Sohn, G. Liu, G.-H. Ryu, and H.-J. Han, 2008: Improvement of microwave rainfall retrievals in Bayesian retrieval algorithms. *J. Meteor. Soc. Japan*, **86** (2), 405–409.
- Shannon, C. E., 1948: A mathematical theory of communication. *Bell System Technical Journal*, **27** (3), 379–423.
- Shannon, C. E., 1956: The bandwagon. *IRE Trans. on Inform. Theory*, **IT** (2), 3.
- Shin, D. and C. Kummerow, 2003: Parametric rainfall retrieval algorithms for passive microwave radiometers. *J. Appl. Meteor.*, **42** (10), 1480–1496.
- Simpson, J., R. Adler, and G. North, 1988: A proposed Tropical Rainfall Measuring Mission (TRMM) satellite. *Bull. Amer. Meteor. Soc.*, **69**, 278–295.
- Smith, E., et al., 1998: Results of WetNet PIP-2 project. *J. Atmos. Sci.*, **55** (9), 1483–1536.
- Smith, E. A., et al., 2007: International Global Precipitation Measurement (GPM) program and mission: An overview. *Measuring Precipitation from Space: EURAIN-SAT and the Future*, Levizzani, V and Bauer, P and Turk, FJ, Ed., Springer, Advances in Global Change Research, Vol. 28, 611+.
- Spencer, R., B. Hinton, and W. Olson, 1983: Nimbus-7 37 GHz radiances correlated with radar rain rates over the Gulf of Mexico. *J. Climate Appl. Meteor.*, **22**, 2095–2099.
- Spencer, R. W., H. M. Goodman, and R. E. Hood, 1989: Precipitation retrieval over

- land and ocean with the SSM/I: identification and characteristics of the scattering signal. *J. Atmos. Ocean Technol.*, **6 (2)**, 254–273.
- Sudradjat, A., N.-Y. Wang, K. Gopalan, and R. R. Ferraro, 2011: Prototyping a generic, unified land surface classification and screening methodology for GPM-era microwave land precipitation retrieval algorithms. *J. Appl. Meteor. Climat.*, **50 (6)**, 1200–1211.
- Tassa, A., S. Di Michele, A. Mugnai, F. S. Marzano, and J. P. V. Poiars Baptista, 2003: Cloud model-based bayesian technique for precipitation profile retrieval from the tropical rainfall measuring mission microwave imager. *Radio Science*, **38 (4)**, doi:10.1029/2002RS002674, URL <http://dx.doi.org/10.1029/2002RS002674>.
- Verdu, S., 2010: viodeolectures.net.
- Wiener, N., 1956: What is information theory? *IRE Trans. on Inform. Theory*, **IT (2)**, 48.
- Wald, A., 1945: Sequential tests of statistical hypotheses. *The Annals of Mathematical Statistics*, **16 (2)**, 117–186.
- Weinman, J. and P. Guetter, 1977: Determination of rainfall distributions from microwave radiation measured by the Nimbus 6 ESMR. *J. Clim. Appl. Meteorol.*, **16**, 437–442.
- Wentz, F., 1998: SSM/I Rain Retrievals within a Unified All-Weather Ocean Algorithm. *J. Atmos. Sci.*, **55 (9)**, 1613–1627.
- Wilheit, T., 1972: *The Electrically Scanning Microwave Radiometer (ESMR) Experiment. Nimbus-5 User's Guide*. NASA/Goddard Space Flight Center.

- Wilheit, T., 1986: Some comments on passive microwave measurement of rain. *Bull. Amer. Meteor. Sci.*, **67**, 1226–1232.
- Wilheit, T., A. Chang, and L. Chiu, 1991: Retrieval of monthly rainfall indices from microwave radiometric measurements using probability distribution functions. *J. Atmos. Ocean. Technol.*, **8 (1)**, 118–136.
- Wilheit, T., A. Chang, M. Rao, E. Rodgers, and J. Theon, 1977: A satellite technique for quantitatively mapping rainfall rates over the oceans. *J. Appl. Meteor.*, **16**, 551–560.
- Wilheit, T., C. Kummerow, and R. Ferraro, 2003: Rainfall algorithms for AMSR-E. *IEEE Trans. Geosci. Remote Sensing*, **41 (2)**, 204–214.
- Xu, Q., 2006: Measuring information content from observations for data assimilation: relative entropy versus shannon entropy difference. *Tellus*, **59A (198-209)**.